석 사 학 위 논 문

Master's Thesis

변형률 평활화 기법을 이용한 3절점 삼각형 쉘 유한요소의 개선

Improvement of a 3-node triangular shell finite element using strain smoothing technique

2017

이 채 민 (李 埰 旻 Lee, Chaemin)

한 국 과 학 기 술 원

Korea Advanced Institute of Science and Technology

석 사 학 위 논 문

변형률 평활화 기법을 이용한 3절점 삼각형 쉘 유한요소의 개선

2017

이 채 민

한 국 과 학 기 술 원

기계항공공학부/기계공학과

변형률 평활화 기법을 이용한 3절점 삼각형 쉘 유한요소의 개선

이 채 민

위 논문은 한국과학기술원 석사학위논문으로
학위논문 심사위원회의 심사를 통과하였음

2016년 12월 16일

심사위원장 이 필 승 (인)

심 사 위 원 이 윤 규 (인)

심 사 위 원 임 세 영 (인)

Improvement of a 3-node triangular shell finite element using strain smoothing technique

Lee, Chaemin

Advisor: Lee, Phill-Seung

A thesis submitted to the faculty of
Korea Advanced Institute of Science and Technology in
partial fulfillment of the requirements for the degree of
Master of Science in Mechanical Engineering

Daejeon, Korea
December 16, 2016

Approved by

Lee, Phill-Seung
Professor of Mechanical Engineering

The study was conducted in accordance with Code of Research Ethics[1)].

1) Declaration of Ethical Conduct in Research**:** I, as a graduate student of Korea Advanced Institute of Science and Technology, hereby declare that I have not committed any act that may damage the credibility of my research. This includes, but is not limited to, falsification, thesis written by someone else, distortion of research findings, and plagiarism. I confirm that my dissertation contains honest conclusions based on my own careful research under the guidance of my advisor.

MME
20153487

Lee, Chaemin. Improvement of a 3-node triangular shell finite element using strain smoothing technique. Department of Mechanical Engineering. 2017. 53+ v pages. Advisor: Lee, Phill-Seung. (Text in English)

Abstract

Shell structures have been widely used in various engineering fields and the Finite Element Method (FEM) has been powerfully used for analyzing these shell structures over the past several decades. Among the various shell finite elements, the triangular shell finite elements are advantageous for automatic mesh generations of shell structures with complex shapes. Even recently a new 3-node triangular shell finite element named MITC3+ has been developed that gives as accurate results as the state-of-the-art 4-node quadrilateral shell finite element. The MITC3+ shell finite element solves the locking phenomenon very successfully and thus has an outstanding convergence behavior in bending-dominated problems. However, there is no difference in membrane performance from the 3-node triangular displacement-based shell finite element (DISP3). In this study, a new 3-node triangular shell finite element named MITC3+S which improves the membrane performance of the MITC3+ shell finite element is proposed and there are two versions. The first version of the MITC3+S shell finite element has contributed to the successful application of the edge-based strain smoothing technique to the continuum mechanics based MITC3+ shell finite element. The first version has successfully improved the membrane performance of the MITC3+ shell finite element. The second version of the MITC3+S shell finite element alleviates the problem of increasing computation time in the first version with an enhanced edge-based strain smoothing technique. The second version has even better membrane performance than the first version.

Keywords FEM, 3-node triangular shell finite element, MITC3+ shell finite element, membrane performance, strain smoothing technique, MITC3+S shell finite element

Contents

List of Tables

List of Figures

Chapter 1. Introduction

Shell structures have been widely used in various engineering fields and Finite Element Method (FEM) has been powerfully used for analyzing these shell structures over the past several decades. The development of a shell finite element which is more reliable and accurate is very important.

Shell structures are 3D structure with one dimension, the thickness, small compared to the other two dimensions and have a curved shape. Due to this curved shape, shell structures can effectively withstand the external forces. Three load-carrying mechanisms of the shell structures are bending action, membrane action and shearing action. As the thickness of a shell structure gets thinner, the shell structure becomes more sensitive and its behavior eventually converges to a specific limit state. This is called the asymptotic behaviors of the shell structures and categorized into membrane-dominated behavior, bending-dominated behavior and mixed behavior depending on shell geometry, boundary condition and loading condition [1].

An ideal shell finite element should satisfy ellipticity, consistency, inf-sup and isotropy condition to have uniform optimal convergence regardless of the three asymptotic behaviors. The most important factor that interferes with the performance of the shell finite elements is the locking that the solution accuracy becomes worse as the shell thickness becomes thinner [2]. To alleviate the locking phenomenon, the Mixed Interpolation of Tensorial Components (MITC) method was developed, which was first applied to quadrilateral shell finite elements and later applied to triangular shell finite elements [3-5].

In general, it is recognized that triangular shell finite elements are advantageous for automatic mesh generations of shell structures with complex shapes but have an insufficient convergence behavior compared to quadrilateral shell finite elements. Therefore, some people have expressed a negative stance on the development of the triangular shell finite elements based on the insufficient convergence behavior of the triangular shell finite elements. But recently, as a result of persistent research, the 3-node triangular shell finite element named MITC3+ was developed that gives as accurate results as the state-of-the-art 4-node quadrilateral shell finite element [6-8].

The MITC3+ shell finite element solves the locking phenomenon very successfully and thus has an outstanding convergence behavior in bending-dominated problems. However, there is no difference in membrane performance from the 3-node triangular displacement-based shell finite element (DISP3). A study to improve the membrane performance of the MITC3+ shell finite element is required.

The purpose of this study is to improve the membrane performance of the MITC3+ shell finite element using the strain smoothing technique. The strain smoothing technique is a particular class of numerical methods for the simulation of physical phenomenon. It was first proposed to eliminate spatial instability in nodal integration for Galerkin mesh-free methods [9] and later expanded to the FEM. An enhanced edge-based strain smoothing technique has been developed and utilized in the process of the study.

In chapter 2, the fundamentals related to the finite element analysis of shell structures are reviewed. The asymptotic behavior of shell structures, the locking behavior and its alleviation, the ideal shell finite element and the basic numerical tests are covered.

In chapter 3, the formulations of the DISP3, MITC3 and MITC3+ shell finite elements are reviewed

In chapter 4, the fundamentals related to the strain smoothing technique are reviewed. The history of the strain smoothing technique, the formulation of the edge-based strain smoothing technique in 2D solid mechanics problems and the result of a simple benchmark problem are covered [10-15].

In chapter 5, the MITC3+S shell finite element is developed and there are two versions. The first version of the MITC3+S shell finite element has contributed to the successful application of the edge-based strain smoothing technique to the continuum mechanics based MITC3+ shell finite element. The first version has successfully improved the membrane performance of the MITC3+ shell finite element. The second version of the MITC3+S shell finite element alleviates the problem of increasing computation time in the first version and has even better membrane performance than the first version.

Chapter 2. Finite element analysis of shell structures

In this chapter, the fundamentals related to the finite element analysis of shell structures are reviewed. The asymptotic behavior of shell structures, the locking behavior and its alleviation, the ideal shell finite element and the basic numerical tests are covered.

2.1. The asymptotic behavior of shell structures

Three load-carrying mechanisms of the shell structures are bending, membrane and shearing actions. Therefore, shell structures under loading have three corresponding deformation energies which are respectively called bending, membrane and shear strain energy. Because the thickness of a shell structure is thin, the shear strain energy can be negligible. Consequentially, the strain energy of a shell structure mainly consists of two parts: membrane and bending strain energy.

As the thickness of a shell structure gets thinner, the shell structure becomes more sensitive and its behavior eventually converges to a specific limit state. This is called the asymptotic behaviors of the shell structures and categorized into membrane-dominated behavior, bending-dominated behavior and mixed behavior depending on shell geometry, boundary condition and loading condition.

It is essential to understand the asymptotic behaviors of the shell structures to accurately interpret the response of the shell structures and to develop an ideal shell finite element. The ideal shell finite element should have uniform optimal convergence regardless of these three asymptotic behaviors. The fundamental asymptotic theory is explained in the following paragraph [1].

The linear Naghdi shell model or Koiter shell model is considered. The general variational form of them is to find

$U^{\varepsilon} \in \Phi$ such that $\varepsilon^3 A_b(U^{\varepsilon}, V) + \varepsilon A_m(U^{\varepsilon}, V) = F^{\varepsilon}(V)$, $\forall V \in \Phi$, (2.1)

where ε is the thickness parameter t / L (t is the thickness and L is the characteristic length of the shell structure, the bilinear form A_b is the scaled bending energy, the bilinear form A_m is, respectively, the scaled membrane energy for the Koiter shell model and the scaled membrane and shear energies for the Naghdi shell model, U^{ε} is the unknown displacement field, V is the test function, Φ is the proper Sobolev space, and F^{ε} is the external loading.

The scaled loading is introduced to define the asymptotic behavior as ε approaches zero:

$$F^{\varepsilon}(V) = \varepsilon^{\rho} G(V), \tag{2.2}$$

in which ρ is the load-scaling factor proven that $1 \le \rho \le 3$.

A space Φ_0 is defined which is the subspace of the pure bending displacements:

$$\Phi_0 = \{V \in \Phi \,|\, A_m(V, V) = 0\}. \tag{2.3}$$

All displacements in Φ_0 correspond to zero membrane and shear energies. If Φ_0 is an empty set, it means that the pure bending is inhibited. On the other hand, if the shell allows non-zero pure bending displacements, it means that the pure bending is non-inhibited. Whether the pure bending is inhibited or not dominantly determines the asymptotic behavior of shells.

If the pure bending is non-inhibited, the shell can have bending-dominated behavior. In the bending-dominated case, the membrane energy term of Equation (2.1) asymptotically vanishes with $\rho = 3$. In conclusion, the general form of the bending-dominated limit problem is to find

$U^0 \in \Phi_0$ such that $A_b(U^0, V) = G(V)$, $\forall V \in \Phi_0$. (2.4)

This limit problem operates only when the loading activates the pure bending displacements. If the loading does not activate the pure bending displacements, the subspace is as follows:

$$G(V) = 0, \ \forall V \in \Phi_0, \tag{2.5}$$

then the solution of the shell problem does not converge to the limit solution of the bending-dominated case, and

instead converges to the limit solutions of the other asymptotic cases, but very unstable.

If the pure bending is inhibited, the shell can have membrane-dominated behavior. In the membrane-dominated case, the bending energy tern of Equation (2.1) asymptotically vanishes with $\rho = 1$. In conclusion, the general form of the membrane-dominated limit problem is to find

$$U^m \in \Phi_m \text{ such that } A_m(U^m, V) = G(V), \ \forall V \in \Phi_m. \tag{2.6}$$

This limit problem operates only when the loading G is in the dual space of Φ_m. The condition $G \in \Phi_m'$ is directly equivalent to

$$\left|G(V)\right| \le C\sqrt{A_m(V,V)}, \ \forall V \in \Phi_m, \tag{2.7}$$

with C a constant. Equation (2.7) ensures that the loading can be resisted by membrane stresses only, and thus the condition $G \in \Phi_m'$ is said to correspond to an admissible loading. If the loading is a non-admissible membrane loading, the solution of the shell problem does not converge to the limit solution of the membrane-dominated case, and instead converges to the limit solutions of a mixed case.

2.2. Locking behavior and its alleviation

In finite element analyses, a convergence rate to the analytical solution severely decreases when the thickness becomes thin during bending-dominated behavior and mixed behavior. This is called locking. The locking occurs because a finite element discretization cannot accurately describe the pure bending displacement field of shells. This phenomenon is usually related to the low order interpolation functions. The types of the locking occurring in shell analysis include membrane locking and transverse shear locking. The membrane locking occurs when there is a curvature on the geometry and on the other hand, the transverse shear locking occurs irrespective of the curvature on the geometry. In the case of the 3-node triangular shell finite elements handled in this study, since these have a flat shape, only the transverse shear locking is considered.

Many methods to alleviate the transverse shear locking have been proposed. First, the RI (Reduced

Integration) and SRI (Selective Reduced Integration) methods were proposed by Zienkiewicz et al. [16]. The RI equally reduces the order of Gauss integration when constructing the stiffness matrix for all the strains. The SRI (Selective Reduced Integration) only reduces the order of Gauss integration when constructing the stiffness matrix for the specific strains that locking occurs. These are very simple to apply, but have a disadvantage of creating spurious modes (hour glass modes). Therefore, stabilization technique should be used together to prevent.

Another method is the DSG (Discrete Shear Gap) method proposed by Bischoff et al. [17,18]. It compares the actual nodal displacements and the displacements corresponding to a pure bending mode. The difference between two displacements is called the shear gap. The shear strains are determined from the interpolated shear gap. This method is applicable to triangles or quadrilateral shell finite elements in the same way.

A third method is the MITC (Mixed Interpolation of Tensorial Components) method proposed by Bathe, et al. It interpolates displacements and strains separately and connects these interpolations at tying points. This method was first used to develop quadrilateral shell finite elements (MITC4, MITC8, MITC9 and MITC16) and later, used to develop triangular shell finite elements (MITC3 and MITC6) [3-5].

In this study, the 3-node triangular shell finite elements are studied. Therefore, the 3-node triangular shell finite element with the DSG method (DSG3) and the 3-node triangular shell finite element with the MITC method (MITC3) need to be examined. Both elements are commonly used and have a quite reasonable convergence behavior. However, while the MITC3 shell finite element gives a stable result and shows an isotropic behavior, the DSG3 shell finite element contains a spurious zero energy mode and shows anisotropic behavior. Also, the DSG3 shell finite element can be only used for flat shell elements [17-19].

For this reason, the MITC method is used to alleviate the locking in this paper. Even recently, the MITC3+ shell finite element has been developed which further develops the MITC3 shell finite element. The MITC3+ shell finite element shows an excellent convergence behavior in bending dominated problems [6-8].

2.3. Ideal shell finite element

An ideal shell finite element should satisfy ellipticity, consistency, inf-sup and isotropy condition to have uniform optimal convergence. Followings are detailed description of each condition [2,5].

- Ellipticity condition indicates that the problem can be solved with the given finite element discretization. This means physically that the shell finite element has no spurious zero energy mode and only has the six zero energy mode corresponding to six rigid body modes.
- Consistency condition indicates that the finite element solution should converge to the solution of the mathematical model as the element size h goes to zero.
- Inf-sup condition indicates that the finite element solution should have uniform optimal convergence in bending dominated problems regardless of the shell thickness, that is, the finite element does not accompany locking phenomenon.
- Isotropy condition indicates that the element stiffness matrices should not depend on the sequence of node numbering.

2.4. Basic numerical tests and convergence studies

Some basic numerical tests are prepared: the isotropy test, the patch tests and the zero energy mode test. These basic numerical tests are requirements to be an ideal shell element, i.e. to satisfy the conditions mentioned in Chapter 2.3. Once a shell finite element is confirmed to pass the basic numerical tests, the convergence studies are next performed. Through the convergence studies, we can confirm whether the consistency and inf-sup conditions are satisfied. The benchmark problems to be used in the convergence studies should be representative of all the asymptotic behaviors and various mesh patterns should be considered. The basic numerical tests are described in the following paragraph [2,5].

For the isotropy test, different node numbering sequences are given as input. Shell finite elements should

give the identical results regardless of the node numbering sequences. For the patch tests, the minimum number of degrees of freedom is constrained to prevent rigid body motions and appropriate loadings are applied to create a constant stress condition. The constant stress must be calculated at all points on the mesh to pass the patch test. Figure 2.1 shows the mesh for all patch tests and the boundary and loading conditions for each patch test. For the zero energy mode test, the number of zero eigenvalues of the stiffness matrix of a single unsupported element are counted. The single shell finite element should pose exactly six zero eigenvalues corresponding to the six physical rigid body modes.

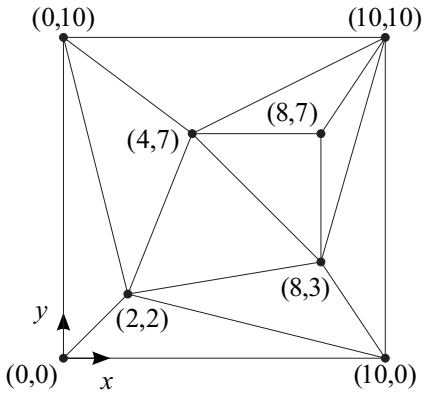

Mesh for patch tests

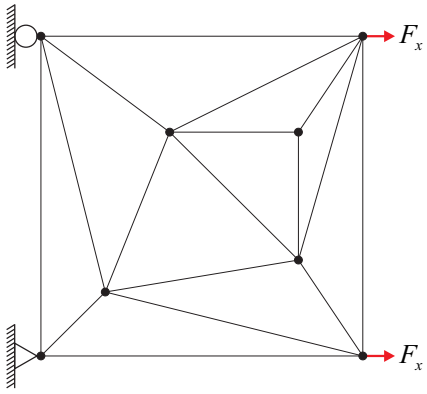

Membrane patch test 1

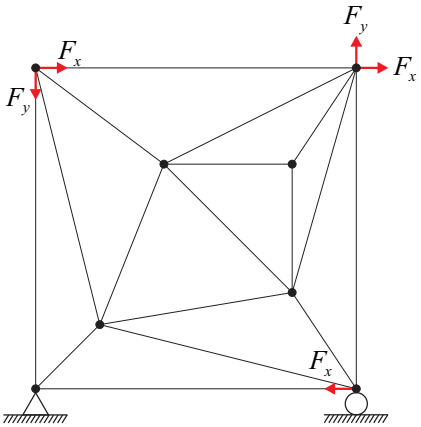

Membrane patch test 2

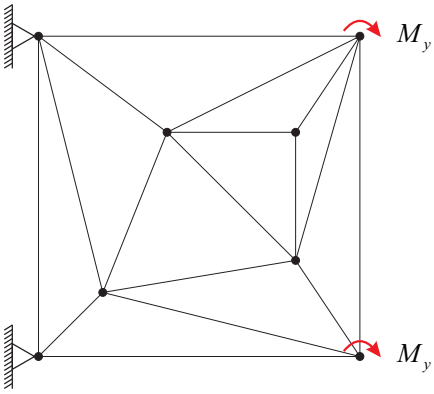

Bending patch test

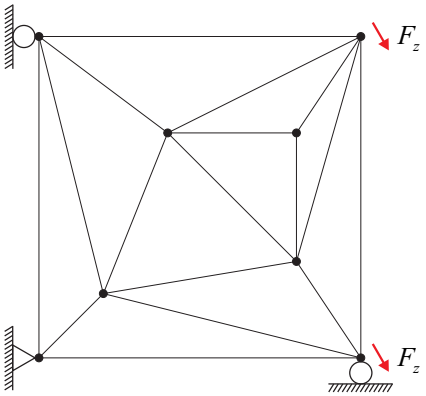

Shearing patch test

Figure 2.1 Mesh for all patch tests and the boundary and loading conditions for each patch test

Chapter 3. 3-node triangular continuum mechanics based shell finite elements

In this chapter, the formulations of the DISP3 shell finite element, the MITC3 shell finite element and the MITC3+ shell finite element are reviewed.

3.1. Formulation of the DISP3 shell finite element

The geometry of the 3-node triangular displacement-based shell finite element is interpolated by [5]

$$\vec{x}(r,s,t) = \sum_{i=1}^{3} h_i(r,s)\vec{x}_i + \frac{t}{2}\sum_{i=1}^{3} a_i h_i(r,s)\vec{V}_n^i \quad \text{with} \quad h_1 = 1-r-s\,,\ h_2 = r\,,\ h_3 = s\,, \tag{3.1}$$

where h_i is the 2D interpolation function of the standard isoparametric procedure corresponding to node i, $\vec{x}_i$ is the position vector at node i in the global Cartesian coordinate system, and a_i and $\vec{V}_n^i$ denote the shell thickness and the director vector at the node i, respectively, see Figure 3.1. Note that the vector $\vec{V}_n^i$ does not have to be normal to the shell midsurface in this description.

The corresponding displacement interpolation of the element is given by

$$\vec{u}(r,s,t) = \sum_{i=1}^{3} h_i(r,s)\vec{u}_i + \frac{t}{2}\sum_{i=1}^{3} a_i h_i(r,s)\left(-\alpha_i \vec{V}_2^i + \beta_i \vec{V}_1^i\right), \tag{3.2}$$

where $\vec{u}_i$ is the nodal displacement vector in the global Cartesian coordinate system, $\vec{V}_1^i$ and $\vec{V}_2^i$ are unit vectors orthogonal to $\vec{V}_n^i$ and to each other, and α_i and β_i are the rotations of the director vector $\vec{V}_n^i$ about $\vec{V}_1^i$ and $\vec{V}_2^i$ at node i.

The linear part of the displacement-based covariant strains is calculated by

$$e_{ij} = \frac{1}{2}(\vec{g}_i \cdot \vec{u}_{,j} + \vec{g}_j \cdot \vec{u}_{,i}), \tag{3.3}$$

where

$$\vec{g}_i = \frac{\partial \vec{x}}{\partial r_i},\ \vec{u}_{,i} = \frac{\partial \vec{u}}{\partial r_i} \text{ with } r_1 = r,\ r_2 = s,\ r_3 = t.$$

The 3-node triangular displacement-based shell finite element passes all basic numerical tests: zero energy mode test, isotropic test and patch tests. However, this shell finite element strongly has the shear locking problem and therefore, it exhibits very extremely stiff behavior in bending-dominated problems.

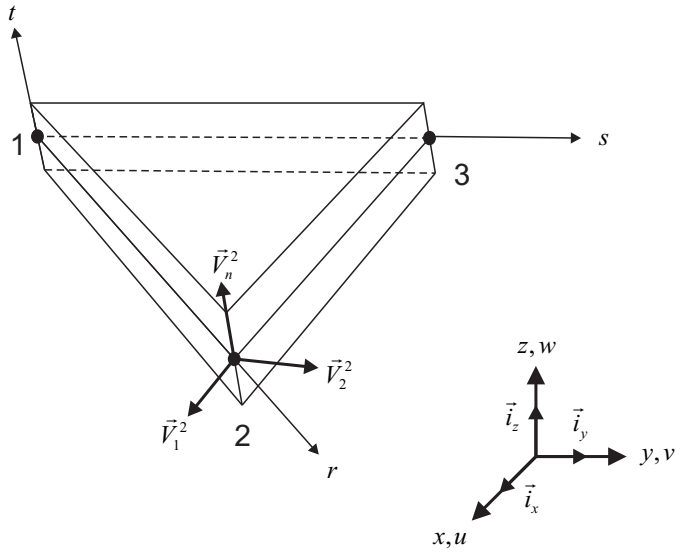

Figure 3.1. A 3-node triangular displacement-based shell finite element

`

3.2. Formulation of the MITC3 shell finite element

The MITC3 shell finite element has the same geometry and displacement interpolations as the DISP3 shell finite element. Instead, the process of constructing assumed covariant transverse shear strain field using the MITC technique is added. It assumes constant covariant transverse shear strains along the edges to construct the assumed covariant transverse shear strain field. The assumed covariant transverse shear strain field and the tying

points of the MITC3 shell finite element are given by [5]

$$e_{rt}^{MITC3} = e_{rt}^{(1)} + cs \,,$$
$$e_{st}^{MITC3} = e_{st}^{(2)} - cr \,, \tag{3.4}$$

where $c = e_{st}^{(2)} - e_{rt}^{(1)} - e_{st}^{(3)} + e_{rt}^{(3)}$, see Figure 3.2 and 3.3.

The MITC3 shell finite element passes all basic numerical tests: zero energy mode test, isotropic test and patch test. In addition, the convergence behavior is also improved to a quite reasonable level. However, there are still some shear locking problems in bending-dominated problems.

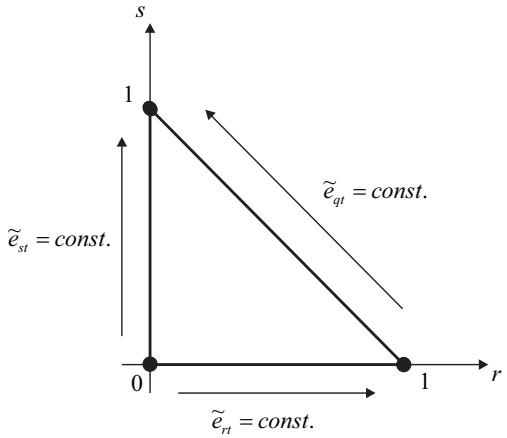

Figure 3.2 Constant transverse shear strain along its edge

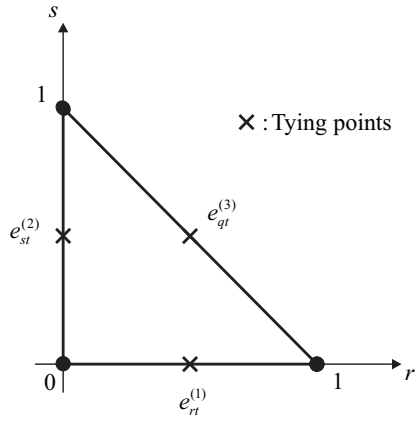

Figure 3.3 Tying positions for the assumed transverse shear strain field

3.3. Formulation of the MITC3+ shell finite element

The MITC3+ shell finite element has bubble node that only has the rotation degrees of freedom on its centroid and also has corresponding cubic bubble function in the geometry and displacement interpolations.

The geometry of the MITC3+ shell finite element is interpolated by [6-8]

$$\vec{x}(r,s,t)=\sum_{i=1}^{3}h_i(r,s)\vec{x}_i+\frac{t}{2}\sum_{i=1}^{4}a_i f_i(r,s)\vec{V}_n^i \quad \text{with} \quad a_4\vec{V}_n^4=\frac{1}{3}\left(a_1\vec{V}_n^1+a_2\vec{V}_n^2+a_3\vec{V}_n^3\right), \tag{3.5}$$

where h_i is the 2D interpolation function of the standard isoparametric procedure corresponding to node i, f_i is the 2D interpolation function with the cubic bubble function:

$$f_1=h_1-\frac{1}{3}f_4,\quad f_2=h_2-\frac{1}{3}f_4,\quad f_3=h_3-\frac{1}{3}f_4,\quad f_4=27rs(1-r-s). \tag{3.6}$$

The corresponding displacement interpolation of the element is given by

$$\vec{u}(r,s,t)=\sum_{i=1}^{3}h_i(r,s)\vec{u}_i+\frac{t}{2}\sum_{i=1}^{4}a_i f_i(r,s)\left(-\alpha_i\vec{V}_2^i+\beta_i\vec{V}_1^i\right), \tag{3.7}$$

where α_4 and β_4 are the rotation degrees of freedom at the bubble node, see Figure 3.4.

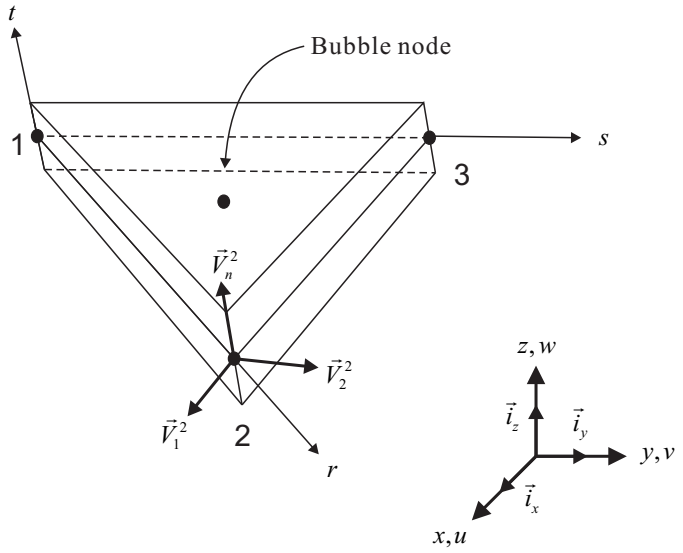

Figure 3.4 Geometry of the MITC3+ shell finite element with an additional bubble node

The assumed covariant transverse shear strain field and the tying points of the MITC3+ shell finite element are given by

$$
\begin{aligned}
e_{rt}^{MITC3+} &= \hat{e}_{rt}^{const.} + \hat{e}_{rt}^{linear} = \frac{2}{3}\left(e_{rt}^{(B)} - \frac{1}{2} e_{st}^{(B)} \right) + \frac{1}{3}\left(e_{rt}^{(C)} + e_{st}^{(C)} \right) + \frac{1}{3}\hat{c}(3s-1), \\
e_{st}^{MITC3+} &= \hat{e}_{st}^{const.} + \hat{e}_{st}^{linear} = \frac{2}{3}\left(e_{st}^{(A)} - \frac{1}{2} e_{rt}^{(A)} \right) + \frac{1}{3}\left(e_{rt}^{(C)} + e_{st}^{(C)} \right) + \frac{1}{3}\hat{c}(1-3r),
\end{aligned}
\tag{3.8}
$$

where $\hat{c} = e_{rt}^{(F)} - e_{rt}^{(D)} - e_{st}^{(F)} + e_{st}^{(E)}$ and the 6 tying points (A)-(F) with the tying distance d in Figure 3.5, 3.6, 3.7 and Table 3.1. The value of d is suggested to be 1/10000.

The MITC3+ shell finite element passes the basic test: zero energy mode, isotropy and patch tests. In addition, the MITC3+ shell finite element shows an excellent convergence behavior in bending-dominated problems.

Table 3.1 Tying positions for the assumed transverse shear strain field for the MITC3+ shell finite element

	Tying points	r	s
Figure 3.6	(A)	1/6	2/3
	(B)	2/3	1/6
	(C)	1/6	1/6
Figure 3.7	(D)	1/3+d	1/3-2d
	(E)	1/3-2d	1/3+d
	(F)	1/3+d	1/3+d

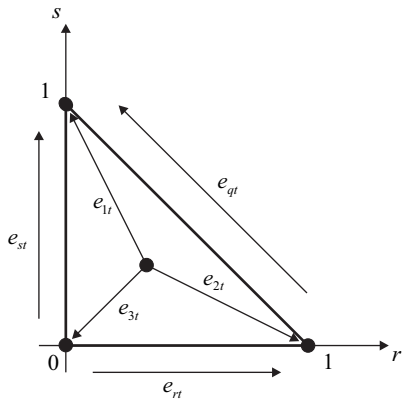

Figure 3.5 Transverse shear strain e_{1t}, e_{2t} and e_{3t}

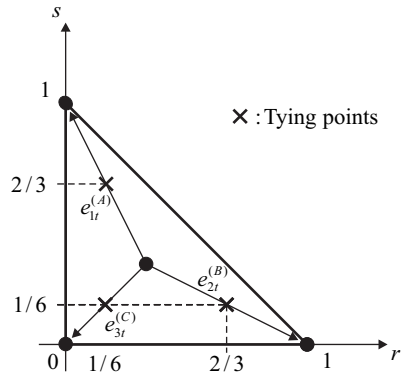

Figure 3.6 Tying positions (A)-(C) for the assumed transverse shear strain field of the MITC3+ shell finite element

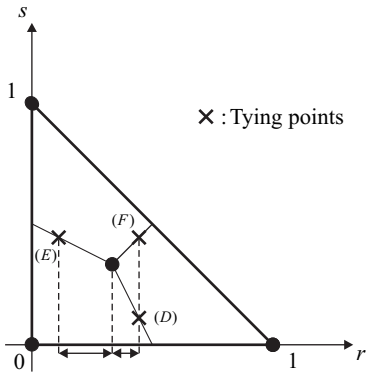

Figure 3.7 Tying positions (D)-(F) for the assumed transverse shear strain field of the MITC3+ shell finite element

Chapter 4. Strain smoothing technique

Strain smoothing technique is a particular class of numerical methods for the simulation of physical phenomenon. The strain smoothing is achieved by modifying (or smoothening) the compatible strain field of the finite elements. This work can be performed within the elements or beyond the elements. In this study, the strain smoothing technique is used to improve the membrane performance of the MITC3+ shell finite element. Therefore, in this chapter, the strain smoothing technique is reviewed first. The history of the strain smoothing technique, the formulation of the edge-based strain smoothing technique in 2D solid mechanics problems and the result of a simple benchmark problem are covered.

4.1. History of the strain smoothing technique

The strain smoothing technique was first proposed by Chen et al. to eliminate spatial instability in nodal integration for Galerkin mesh-free methods [9] and later has expanded to the FEM. For the finite element analyses in 2D solid mechanics problems, the edge-based strain smoothing technique and the node-based strain smoothing technique were proposed by Liu et al [10,11]. In the case of the node-based strain smoothing technique, the strain smoothing domain is created by connecting sequentially the mid-edge points to the centroids of the surrounding elements. The node-based strain smoothing gives upper bound in the strain energy of the solution and is immune from the volumetric locking [10]. In the case of the edge-based strain smoothing technique, the strain smoothing domain is created by connecting sequentially the two end points of the edge to the two centroids of the two surrounding elements. The edge-based strain smoothing using triangular finite elements give more stable and accurate solution than the conventional FEM and doesn't cause the increase in degrees of freedom [11]. The strain smoothing technique has been extended to plate and shell elements. Most of them used with the DSG method [12-14]. The strain smoothing technique has been also applied to develop effective schemes for the finite element analyses in 3D solid mechanics problems [16,17].

4.2. Formulation of the edge-based strain smoothing technique in 2D solid mechanics problems

In this study, the concept of the edge-based strain smoothing technique is used among the various strain smoothing techniques. The edge-based strain smoothing technique is more efficient and gives more successful results when used for the 3-node triangular finite elements than other strain smoothing techniques. The formulation of the edge-based strain smoothing technique in 2D solid mechanics problems is reviewed below.

The formulation of the edge-based strain smoothing technique basically starts from that of the FEM. First, the compatible strain fields have to be obtained through the FEM procedures [2], then smoothed strain fields are constructed with the edge-based strain smoothing technique [11].

The basis of the displacement-based finite element solution is the principle of virtual work. This principle states that the equilibrium of the body requires that the total inner virtual work is equal to the total external virtual work for any compatible small virtual displacements imposed on the body in its equilibrium condition:

$$\int_V \delta\vec{\bar{\varepsilon}}^{\mathrm{T}}\vec{\bar{\tau}}dV = \int_V \delta\vec{u}^{\mathrm{T}}\vec{f}^{B}dV + \int_{S_f} \delta\vec{u}^{S_f\,\mathrm{T}}\vec{f}^{S_f}dS + \sum_i \delta\vec{u}^{i\,\mathrm{T}}\vec{R}_C^i \,, \tag{4.1}$$

where $\delta\vec{u}$ are the virtual displacements and $\delta\vec{\bar{\varepsilon}}$ are the corresponding virtual strains.

In the finite element analyses, a body is approximated as an assemblage of discrete finite elements interconnected at nodal points on the boundaries of elements. The displacements within each element are assumed to be a function of the displacements at the nn nodal points:

$$\vec{u} = \sum_{i=1}^{nn} \mathbf{H}_i \vec{u}_i \,, \tag{4.2}$$

where $\vec{u}_i$ is the nodal displacement vector and $\mathbf{H}_i = \begin{bmatrix} h_i & 0 \\ 0 & h_i \end{bmatrix}$ is the displacement interpolation matrix.

Then the corresponding strains within each element are obtained by using the assumption on the displacements in Equation (4.1):

$$\vec{\varepsilon} = \sum_{i=1}^{nn} \mathbf{B}_i \vec{u}_i \,, \tag{4.3}$$

where $\mathbf{B}_i = \begin{bmatrix} h_{i,x} & 0 \\ 0 & h_{i,y} \\ h_{i,y} & h_{i,x} \end{bmatrix}$ is the strain-displacement matrix. The rows of the $\mathbf{B}_i$ are obtained by appropriately differentiating and combining the rows of the $\mathbf{H}_i$.

To construct the smoothed strain fields, the compatible strains obtained from the conventional FEM are smoothed over local strain smoothing domains. The local strain smoothing domains are constructed based on the edges of elements.

The smoothed strains can be obtained by

$$\tilde{\varepsilon}_k = \int_{\Omega^{(k)}} \varepsilon(x) \phi_k(x) \, \mathrm{d}\Omega \;\text{ with }\; \phi_k(x) = \begin{cases} 1/A^{(k)}, & x \in \Omega^{(k)} \\ 0, & x \notin \Omega^{(k)} \end{cases}, \tag{4.4}$$

where $\Omega^{(k)}$ is the smoothing domain associated with the k th edge and $A^{(k)}$ is the area of the $\Omega^{(k)}$.

The area of the smoothing domain associated with the k th edge $A^{(k)}$ is calculated by

$$A^{(k)} = \int_{\Omega^{(k)}} \mathrm{d}\Omega = \frac{1}{3} \sum_{j=1}^{ne^{(k)}} A_e^{(j)} \,, \tag{4.5}$$

where $A_e^{(j)}$ is the area of the j th element around the k th edge and $ne^{(k)}$ is the number of elements around the k th edge, i.e. $ne^{(k)} = 1$ for the boundary edges and $ne^{(k)} = 2$ for the inner edges.

The matrix form of the smoothed strains on the domain $\Omega^{(k)}$ can be written by

$$\tilde{\varepsilon}_k = \sum_{i \in nn^{(k)}} \tilde{\mathbf{B}}_i \vec{u}_i \,, \tag{4.6}$$

where $\tilde{\mathbf{B}}_i$ is the smoothed strain-displacement matrix, $\vec{u}_i$ is the nodal displacement vector and $nn^{(k)}$ is the

total number of nodes in the smoothing domain $\Omega^{(k)}$, i.e. $nn^{(k)} = 3$ for the boundary edges and $nn^{(k)} = 4$ for the inner edges.

The smoothed strain-displacement matrix $\widetilde{\mathbf{B}}_i$ is obtained numerically by

$$\widetilde{\mathbf{B}}_i = \frac{1}{A^{(k)}} \sum_{j=1}^{ne^{(k)}} \frac{1}{3} A_e^{(j)} \mathbf{B}_j , \tag{4.7}$$

where $\mathbf{B}_j$ is the strain-displacement matrix of the j th element around the k th edge.

The strain fields of 3-node triangular finite elements changes from Figure 4.1 to Figure 4.2 when the edge-based strain smoothing technique is applied. Through this chapter, we have confirmed that the formulation of the edge-based strain smoothing technique for the 3-node triangular finite elements is very clear and easy to implement.

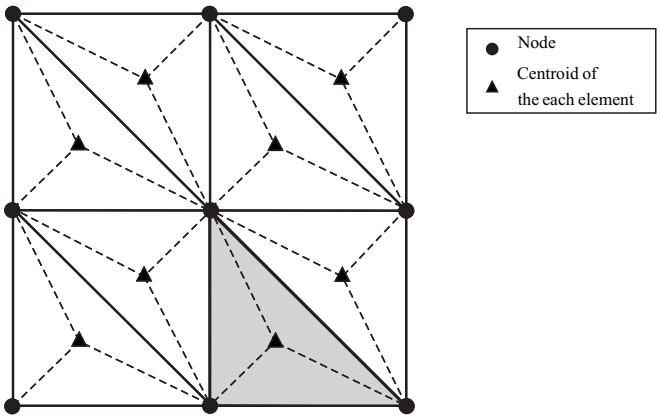

Figure 4.1 Membrane strain field of the original 3-node triangular finite element

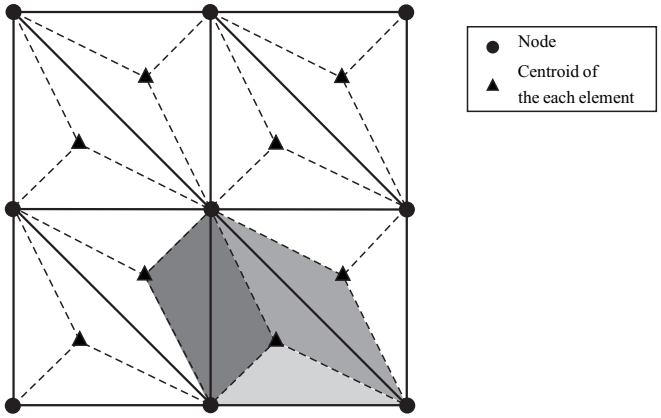

Figure 4.2 Membrane strain field of the edge-based strain smoothed 3-node triangular finite element

4.3. Basic numerical tests

In this chapter, the three basic numerical tests are considered: the isotropy test, the patch tests and the zero energy mode test. The details about the basic numerical tests are given in Chapter 2.4 and Figure 2.1.

The isotropy test is performed. The smoothed 3-node triangular finite element gives the identical results regardless of the node numbering sequences. The membrane patch test is performed. The smoothed 3-node triangular finite element gives a constant stress at all points on the mesh. The zero energy mode test is performed. The smoothed 3-node triangular finite element poses exactly three zero eigenvalues corresponding to the three physical rigid body modes. In conclusion, the smoothed 3-node triangular finite element passes all the basic numerical tests.

4.4. Convergence studies

In this chapter, a simple convergence study is performed to demonstrate the effectiveness of the edge-based strain smoothing technique in 2D solid mechanics problems.

The numerical example, 'a cantilever subjected to a parabolic traction at the free end', is considered [11]. This cantilever has a length of L, a height of D and a unit thickness so that plane stress condition is valid, see Figure 4.3.

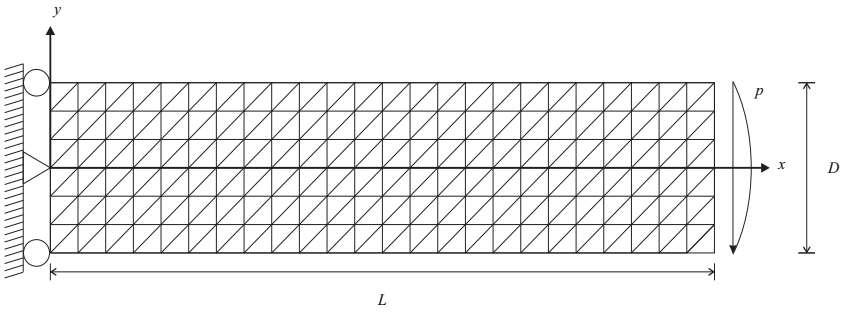

Figure 4.3 A cantilever subjected to a parabolic traction at the free end

The analytical solution of this problem is given by [22]

$$u_x = \frac{Py}{6EI}\left[(6L-3x)x+(2+\nu)\left(y^2-\frac{D^2}{4}\right)\right],$$
$$u_y = -\frac{P}{6EI}\left[3\nu y^2(L-x)+(4+5\nu)\frac{D^2x}{4}+(3L-x)x^2\right], \tag{4.8}$$

where I is the moment of inertia.

The stresses corresponding to the displacements are

$$\sigma_{xx}(x,y)=\frac{P(L-x)y}{I},\ \sigma_{yy}(x,y)=0,\ \tau_{xy}(x,y)=-\frac{P}{2I}\left(\frac{D^2}{4}-y^2\right). \tag{4.9}$$

The loading on the right end ($x = L$) uses the exact distributed stresses from Equation (4.9). The properties are as follows: $E = 3.0\times10^7$ Pa , $\nu = 0.3$, $L = 48$ m , $D = 12$ m and $P = 1000$ N .

Figure 4.4 gives the y direction displacements, v , at the midline ($x = 0$) of the conventional 2D 3-node triangular finite element, the edge-based strain smoothed 2D 3-node triangular finite element and the

analytical solution. The edge-based strain smoothed 2D 3-node triangular finite element gives a result almost identical to the analytical solution.

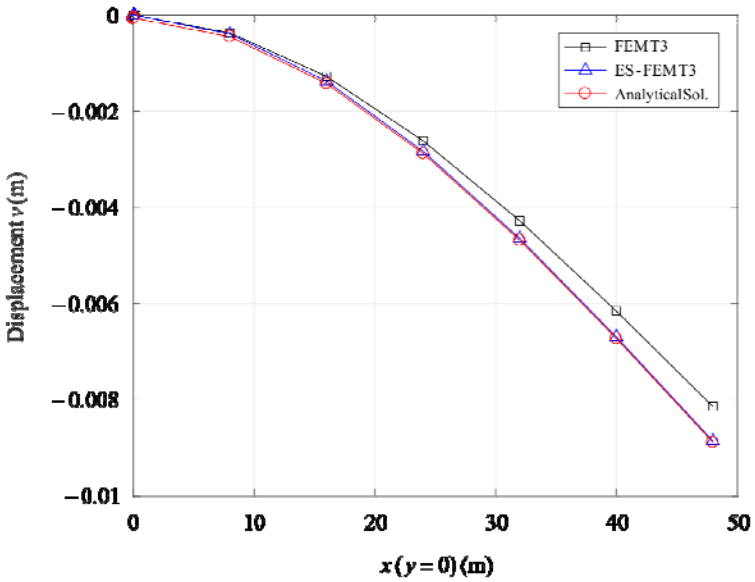

Figure 4.4 Distribution of displacement v along (x , 0)

Chapter 5. MITC3+S shell finite element

In chapter 5, the MITC3+S shell finite element is developed and there are two versions. The first version of the MITC3+S shell finite element is explained in Chapter 5.1. The first version has contributed to the successful application of the edge-based strain smoothing technique to the continuum mechanics based MITC3+ shell finite element. The first version has successfully improved the membrane performance of the MITC3+ shell finite element. The second version of the MITC3+S shell finite element is explained in Chapter 5.2. The second version alleviates the problem of increasing computation time in the first version and has even better membrane performance than the first version.

5.1. Development of the first version of the MITC3+S shell finite element

In the formulation of the MITC3+S shell finite element, the mid-surface of the element is subdivided into three 3-node triangular domains using the three edges and the centroid of the element. This divided domains are called cells and the membrane strain fields are newly constructed based on the cells. In 2D solid mechanics problems, it can be said that the strain fields are reconstructed based on the edges, but it is more accurate that the strain fields are reconstructed based on the cells in shell problems because shell elements are not always present in the same plane. Followings are the formulation of the MITC3+S shell finite element.

The geometry of the MITC3+ shell finite element is interpolated by [6-8]

$$\vec{x}(r,s,t)=\sum_{i=1}^{3}h_i(r,s)\vec{x}_i+\frac{t}{2}\sum_{i=1}^{4}a_i f_i(r,s)\vec{V}_n^i \quad \text{with} \quad a_4\vec{V}_n^4=\frac{1}{3}\left(a_1\vec{V}_n^1+a_2\vec{V}_n^2+a_3\vec{V}_n^3\right), \tag{5.1}$$

where h_i is the 2D interpolation function of the standard isoparametric procedure corresponding to node i, f_i is the 2D interpolation function with the cubic bubble function:

$$f_1=h_1-\frac{1}{3}f_4,\quad f_2=h_2-\frac{1}{3}f_4,\quad f_3=h_3-\frac{1}{3}f_4,\quad f_4=27rs(1-r-s). \tag{5.2}$$

The corresponding displacement interpolation of the element is given by

$$\vec{u}(r,s,t)=\sum_{i=1}^{3}h_i(r,s)\vec{u}_i+\frac{t}{2}\sum_{i=1}^{4}a_i f_i(r,s)\left(-\alpha_i\vec{V}_2^{\,i}+\beta_i\vec{V}_1^{\,i}\right), \tag{5.3}$$

where α_4 and β_4 are the rotation degrees of freedom at the bubble node, see Figure 3.4.

The linear part of the displacement-based covariant strains is calculated by

$$e_{ij}=\frac{1}{2}(\vec{g}_i\cdot\vec{u}_{,j}+\vec{g}_j\cdot\vec{u}_{,i}), \tag{5.4}$$

where

$\vec{g}_i=\dfrac{\partial\vec{x}}{\partial r_i}$ and $\vec{u}_{,i}=\dfrac{\partial\vec{u}}{\partial r_i}$ with $r_1=r$, $r_2=s$, $r_3=t$.

The MITC3+ shell finite element solves the locking phenomenon very successfully and thus has an outstanding convergence behavior in bending-dominated problems. This is achieved by properly assuming the covariant transverse shear strains using the MITC method. Therefore, in this study, the assumed covariant transverse shear strains of the MITC3+ shell finite element is employed and only the covariant membrane strains are smoothed using the strain smoothing technique.

The covariant membrane strains can be decomposed by [23]

$$e_{ij}^{in-plane}=e_{ij}^{m}+te_{ij}^{b1}+t^2e_{ij}^{b2} \text{ with } i,j=1,2, \tag{5.5}$$

$$e_{ij}^{m}=\frac{1}{2}\left(\frac{\partial\vec{x}_m}{\partial r_i}\cdot\frac{\partial\vec{u}_m}{\partial r_j}+\frac{\partial\vec{x}_m}{\partial r_j}\cdot\frac{\partial\vec{u}_m}{\partial r_i}\right), \tag{5.6}$$

$$e_{ij}^{b1}=\frac{1}{2}\left(\frac{\partial\vec{x}_m}{\partial r_i}\cdot\frac{\partial\vec{u}_b}{\partial r_j}+\frac{\partial\vec{x}_m}{\partial r_j}\cdot\frac{\partial\vec{u}_b}{\partial r_i}+\frac{\partial\vec{x}_b}{\partial r_i}\cdot\frac{\partial\vec{u}_m}{\partial r_j}+\frac{\partial\vec{x}_b}{\partial r_j}\cdot\frac{\partial\vec{u}_m}{\partial r_i}\right), \tag{5.7}$$

$$e_{ij}^{b2}=\frac{1}{2}\left(\frac{\partial\vec{x}_b}{\partial r_i}\cdot\frac{\partial\vec{u}_b}{\partial r_j}+\frac{\partial\vec{x}_b}{\partial r_j}\cdot\frac{\partial\vec{u}_b}{\partial r_i}\right) \tag{5.8}$$

$$\text{with } \vec{x}_m = \sum_{i=1}^{3} h_i(r,s)\vec{x}_i \,,\ \vec{x}_b = \frac{1}{2}\sum_{i=1}^{4} a_i f_i(r,s)\vec{V}_n^{\,i} \,,$$
$$\vec{u}_m = \sum_{i=1}^{3} h_i(r,s)\vec{u}_i \,,\ \vec{u}_b(r,s) = \frac{1}{2}\sum_{i=1}^{4} a_i f_i(r,s)(-\alpha_i \vec{V}_2^{\,i} + \beta_i \vec{V}_1^{\,i}) \,, \tag{5.9}$$

in which $e_{ij}^{in-plane}$ is the covariant in-plane strains, e_{ij}^{m} is the covariant membrane strains and the other terms are the covariant bending strains. The covariant membrane strains have a constant value in each element. Since only the strain smoothing is applied to the covariant membrane strains, only the translation degrees of freedom is considered during the strain smoothing procedures.

In the case of shells, two neighboring elements are not always present in the same plane, which means the two neighboring elements lie on different coordinate systems. Therefore, to enable the strain smoothing between the two neighboring elements lying on different planes, a new local Cartesian coordinate system is required. Two types of the new local Cartesian coordinate systems are tested. The first type has already been used to apply the strain smoothing technique to flat shell elements [14,15].

A common local Cartesian coordinate system is defined in the case of the first type. The base vectors $\tilde{\vec{L}}_i^k$ are obtained by

$$\tilde{\vec{L}}_3^k = \frac{\vec{n} + \vec{n}^{\,ADJ.}}{\left\| \vec{n} + \vec{n}^{\,ADJ.} \right\|} \,, \tag{5.10}$$

$$\tilde{\vec{L}}_1^k = \tilde{\vec{L}}_2^k \times \tilde{\vec{L}}_3^k \,, \tag{5.11}$$

where the right superscript k denotes the k th cell of the element, $\tilde{\vec{L}}_2^k$ is the unit vector tangential to the k th edge of the element, $\vec{n}$ is the vector normal to the element and $\vec{n}^{\,ADJ.}$ is the vector normal to the adjacent element, see Figure 5.1.

Two different local Cartesian coordinate systems are defined in the case of the second type. The base vectors $\tilde{\vec{L}}_i^k$ and ${}^{ADJ.}\tilde{\vec{L}}_i^k$ are obtained by

$$\vec{\tilde{L}}_1^k = \vec{\tilde{L}}_2^k \times \vec{\tilde{L}}_3^k , \tag{5.12}$$

$$^{ADJ.}\vec{\tilde{L}}_1^k = {}^{ADJ.}\vec{\tilde{L}}_2^k \times {}^{ADJ.}\vec{\tilde{L}}_3^k , \tag{5.13}$$

where the right superscript k denotes the k th cell of the element or the adjacent element, $\vec{\tilde{L}}_2^k$ and $^{ADJ.}\vec{\tilde{L}}_2^k$ are the unit vectors tangential to the k th edge of the element and $\vec{\tilde{L}}_3^k$ and $^{ADJ.}\vec{\tilde{L}}_3^k$ are the unit vectors normal to the element and the adjacent element, respectively, see Figure 5.2.

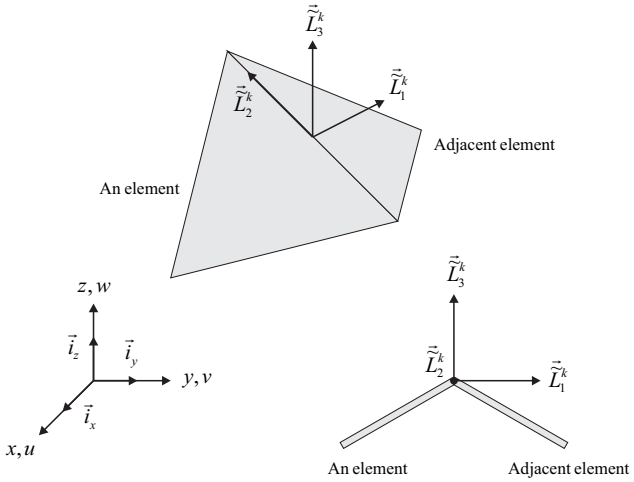

Figure 5.1 A common local Cartesian coordinate system for strain smoothing

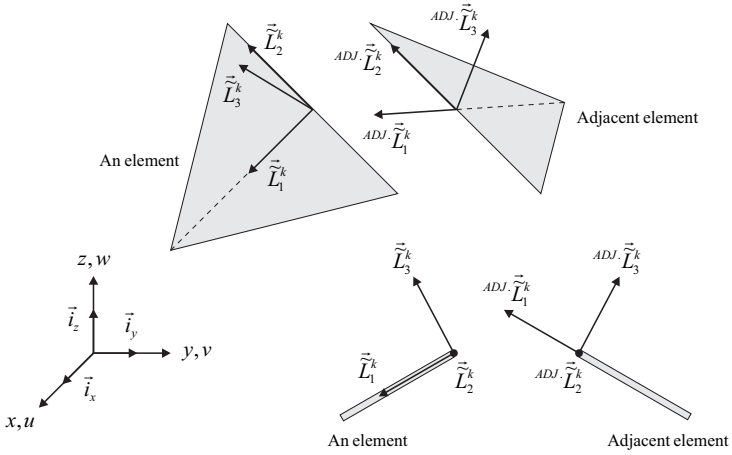

Figure 5.2 Two different local Cartesian coordinate systems for strain smoothing

When the covariant membrane strains of the element and the adjacent element are transformed to the strains for the common local Cartesian coordinate system, transverse shear strains can be generated. In this case, the strain smoothing should be applied to all the strain components including the transverse shear strains. When the covariant membrane strains of the element and the adjacent element are transformed to the strains for the two different local Cartesian coordinate systems, respectively, transverse shear strains are not generated. In this case, the strain smoothing is applied only to the membrane strain components. Both types give almost the same results, but the second type is advantageous in computation time. Therefore, the second type is used in this study.

The local strains of the element ε_{mn} and the local strains of the adjacent element ${}^{ADJ.}\varepsilon_{mn}$ that transforms the covariant membrane strains of the element and the adjacent element for the two different local Cartesian coordinate systems, respectively, are obtained by

$$\varepsilon_{mn} = e_{ij}^{m}(\bar{\bar{L}}_{m}^{k} \cdot \vec{g}^{\,i})(\bar{\bar{L}}_{n}^{k} \cdot \vec{g}^{\,j}), \tag{5.14}$$

$${}^{ADJ.}\varepsilon_{mn} = {}^{ADJ.}e_{ij}^{m}({}^{ADJ.}\bar{\bar{L}}_{m}^{k} \cdot \vec{g}^{\,i})({}^{ADJ.}\bar{\bar{L}}_{n}^{k} \cdot \vec{g}^{\,j}), \tag{5.15}$$

in which e_{ij}^{m} are the covariant membrane strains of the element and ${}^{ADJ.}e_{ij}^{m}$ are the covariant membrane strains of the adjacent element.

The local strains of the element and the adjacent element can be written in the following matrix form:

$$\varepsilon_{mn} = \mathbf{B}_{mn}\vec{u}^{(e)}, \tag{5.16}$$

$${}^{ADJ.}\varepsilon_{mn} = {}^{ADJ.}\mathbf{B}_{mn}\,{}^{ADJ}\vec{u}^{(e)}, \tag{5.17}$$

in which $\mathbf{B}_{mn}$ is the strain-displacement matrix corresponding to the local strains of the element, ${}^{ADJ.}\mathbf{B}_{mn}$ is the strain-displacement matrix corresponding to the local strains of the adjacent element, $\vec{u}^{(e)}$ is the nodal displacement vector of the element and ${}^{ADJ.}\vec{u}^{(e)}$ is the nodal displacement vector of the adjacent element.

However, the above matrix representation is not suitable to apply the strain smoothing technique. Instead, it can be expressed as

$$\varepsilon_i = \mathbf{B}_i \vec{u}_i^{(e)}, \tag{5.18}$$

$$^{ADJ.}\varepsilon_i = {}^{ADJ.}\mathbf{B}_i \, {}^{ADJ.}\vec{u}_i^{(e)}, \tag{5.19}$$

in which ε_i is the local strains corresponding to the i th node of the element, $^{ADJ.}\varepsilon_i$ is the local strains corresponding to the i th node of the adjacent element, $\mathbf{B}_i$ is the strain-displacement matrix corresponding to the i th node of the element, $^{ADJ.}\mathbf{B}_i$ is the strain-displacement matrix corresponding to the i th node of the adjacent element, $\vec{u}_i^{(e)}$ is the i th nodal displacement vector of the element and $^{ADJ.}\vec{u}_i^{(e)}$ is the i th nodal displacement vector of the adjacent element.

The smoothed local strains can be obtained by

$$\widetilde{\varepsilon}_k = \int_{\Omega^{(k)}} \varepsilon(x)\phi_k(x)\, \mathrm{d}\Omega \text{ with } \phi_k(x) = \begin{cases} 1/A^{(k)}, & x \in \Omega^{(k)} \\ 0, & x \notin \Omega^{(k)} \end{cases}, \tag{5.20}$$

where $\Omega^{(k)}$ is the smoothing domain associated with the k th edge and $A^{(k)}$ is the area of the $\Omega^{(k)}$.

The area of the smoothing domain associated with the k th edge is calculated by

$$A^{(k)} = \int_{\Omega^{(k)}} \mathrm{d}\Omega = \frac{1}{3}\sum_{j=1}^{ne^{(k)}} A_e^{(j)}, \tag{5.21}$$

where $A_e^{(j)}$ is the area of the j th element around the k th edge and $ne^{(k)}$ is the number of elements around the k th edge, i.e. $ne^{(k)} = 1$ for the boundary edges and $ne^{(k)} = 2$ for the inner edges.

The matrix form of the smoothed strains on the domain $\Omega^{(k)}$ can be written by

$$\widetilde{\varepsilon}_k = \sum_{i \in nn^{(k)}} \widetilde{\mathbf{B}}_i \vec{u}_i, \tag{5.22}$$

where $\widetilde{\mathbf{B}}_i$ is the smoothed strain-displacement matrix, $\vec{u}_i$ is the nodal displacement vector and $nn^{(k)}$ is the total number of nodes in the smoothing domain $\Omega^{(k)}$, i.e. $nn^{(k)} = 3$ for the boundary edges and $nn^{(k)} = 4$ for the inner edges.

The smoothed strain-displacement matrix $\widetilde{\mathbf{B}}_i$ is obtained numerically by

$$\widetilde{\mathbf{B}}_i = \frac{1}{A^{(k)}} \sum_{j=1}^{ne^{(k)}} \frac{1}{3} A_e^{(j)} \mathbf{B}_j , \tag{5.23}$$

where $\mathbf{B}_j$ is the strain-displacement matrix of the j th element around the k th edge, i.e. $\mathbf{B}_1$ is the strain-displacement matrix of the element and $\mathbf{B}_2$ is the strain-displacement matrix of the adjacent element.

After the strain smoothing procedures, the smoothed local strains are transformed to the smoothed covariant membrane strains for the corresponding contravariant base vectors:

$$(\widetilde{e}_k^m)_{ij} = (\widetilde{\varepsilon}_k)_{mn} (\vec{g}_i \cdot \vec{\widetilde{L}}_m^k)(\vec{g}_j \cdot \vec{\widetilde{L}}_n^k) , \tag{5.24}$$

where $\widetilde{\varepsilon}_k$ is the smoothed local strains on the domain $\Omega^{(k)}$, $\widetilde{e}_k^m$ is the smoothed covariant membrane strains which transforms the $\widetilde{\varepsilon}_k$ for the corresponding contravariant coordinate system.

In conclusion, the smoothed covariant membrane strains replace the original covariant membrane strains and the assumed covariant transverse shear strains of the MITC3+ shell finite element replace the original covariant transverse shear strains.

Then, the new covariant strains are transformed for the Cartesian shell-aligned coordinate system for the numerical integration of the stiffness matrix. In the case of the MITC3+ shell finite element, the numerical integration of the stiffness matrix is performed based on an element:

$$\mathbf{K}^{(e)} = \int_{V^{(e)}} \overline{\mathbf{B}}^{\mathrm{T}} \overline{\mathbf{C}} \overline{\mathbf{B}} dV = \frac{1}{2} \sum_{i=1}^{N_p} \sum_{j=1}^{N_t} w_i \hat{w}_j \overline{\mathbf{B}}^{\mathrm{T}} \overline{\mathbf{C}} \overline{\mathbf{B}} \det \mathbf{J} , \tag{5.25}$$

where $V^{(e)}$ is the volume of the element, N_t is the number of Gauss points for the thickness direction, N_p is the number of Gauss points for the surface, w_i is the i th Gauss weights for the thickness direction, $\hat{w}_j$ is the j th Gauss weights for the surface, $\overline{\mathbf{C}}$ is the material matrix, $\det \mathbf{J}$ is the determinant of the Jacobian transforming global to natural coordinate system and $\overline{\mathbf{B}}$ is the strain-displacement matrix of the local strains that transforms the covariant strains for the Cartesian shell-aligned coordinate system. The MITC3+ shell finite

element requires $N_p = 7$ due to the cubic bubble function and $N_t = 2$, see Figure 5.3.

However, after the strain smoothing procedures, the numerical integration of the stiffness matrix is performed based on a cell:

$$\mathbf{K}^{(e)} = \sum_{k=1}^{nc} \int_{V_k^{(e)}} \overline{\widetilde{\mathbf{B}}}_k^{\mathrm{T}} \overline{\mathbf{C}} \overline{\widetilde{\mathbf{B}}}_k dV = \sum_{k=1}^{nc} \frac{1}{2} \sum_{i=1}^{N_p} \sum_{j=1}^{N_t} w_i w_j \overline{\widetilde{\mathbf{B}}}_k^{\mathrm{T}} \overline{\mathbf{C}} \overline{\widetilde{\mathbf{B}}}_k \frac{1}{3} \det \mathbf{J} \,, \tag{5.26}$$

where nc is the number of the cells in an element, i.e. $nc = 3$ in the case of triangular shell finite elements, $V_k^{(e)}$ is the volume of the k th cell, $\overline{\widetilde{\mathbf{B}}}_k$ is the strain-displacement matrix of the local strains that transforms the new covariant strains of the k th cell for the Cartesian shell-aligned coordinate system.

The first version of the MITC3+S shell finite element contributed to the successful application of the edge-based strain smoothing technique to the continuum mechanics based MITC3+ shell finite element. The first version has successfully improved the membrane performance of the MITC3+ shell finite element.

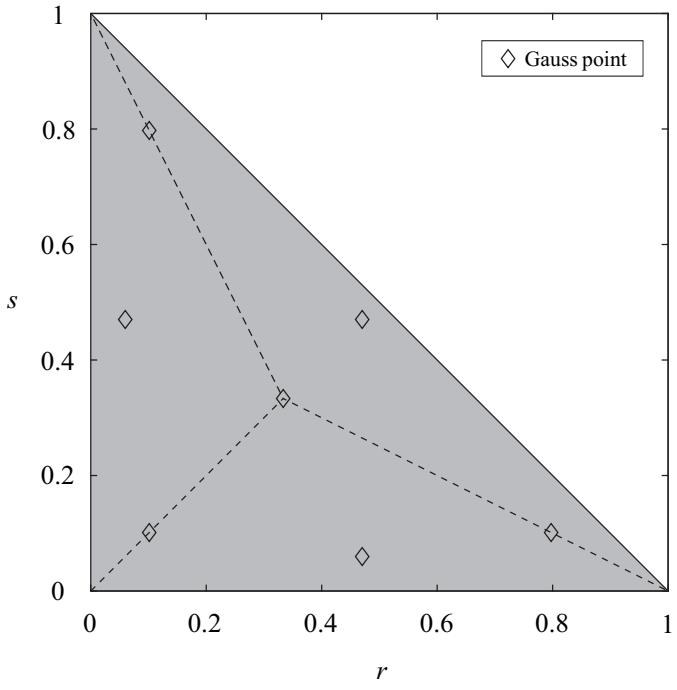

Figure 5.3 The membrane strain fields of the MITC3+ shell finite element and the spatial distribution of 7 Gauss points that the MITC3+ shell finite element uses

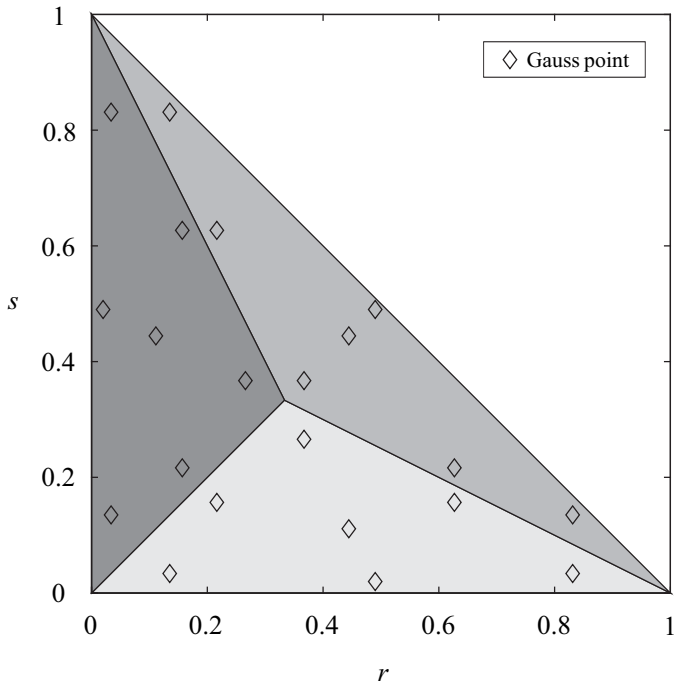

Figure 5.4 The membrane strain fields of the MITC3+S shell finite element (ver. 1) and the spatial distribution of the 21 Gauss points that the MITC3+S shell finite element (ver. 1) uses

5.2. Development of the second version of the MITC3+S shell finite element using an enhanced edge-based strain smoothing technique

The first version of the MITC3+S shell finite element doesn't increase the number of degrees of freedom, but instead increases the number of the integration points by 3 times, see Figure 5.4. This is not fatal, but it certainly increases the computation time. Therefore, the second version of the MITC3+S shell finite element has been developed which alleviates the problem of increasing computation time in the first version and has even better membrane performance than the first version. An enhanced edge-based strain smoothing technique has been developed and utilized in the process of the study.

Figure 5.5 shows the membrane strain fields of the first type of the MITC3+S shell finite element and the spatial distribution of the 7 Gauss points that the MITC3+ shell finite element uses. Fundamentally the 7 Gauss

points can't be used for the first type of the MITC3+S shell finite element because of the Gauss points located at the boundaries between the cells.

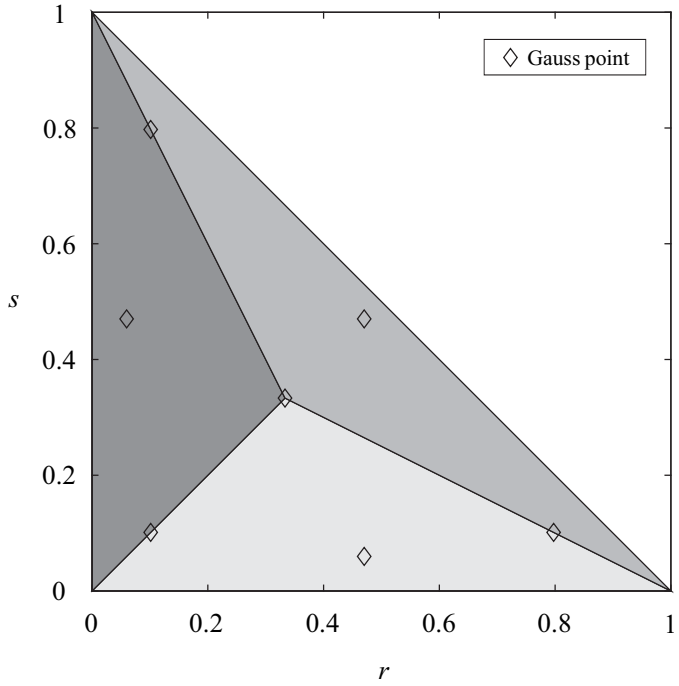

Figure 5.5 The membrane strain fields of the MITC3+S shell finite element (ver. 1) and the spatial distribution of the 7 Gauss points that the MITC3+ shell finite element uses

The enhanced edge-based strain smoothing technique uses these 3 Gauss points located at the boundaries between the cells. Specifically, one more strain smoothing is performed at the 3 Gauss points located at the boundaries, i.e. for the Gauss points located at the boundaries between two cells, the averaged value of the two neighboring cells' once smoothed covariant membrane strains are used, and for the Gauss points located at the centroid, the averaged value of the all cells' once smoothed covariant membrane strains are used, see Figure 5.6.

The second version of the MITC3+S shell finite element alleviates the problem of increasing computation time in the first version and has even better membrane performance than the first version.

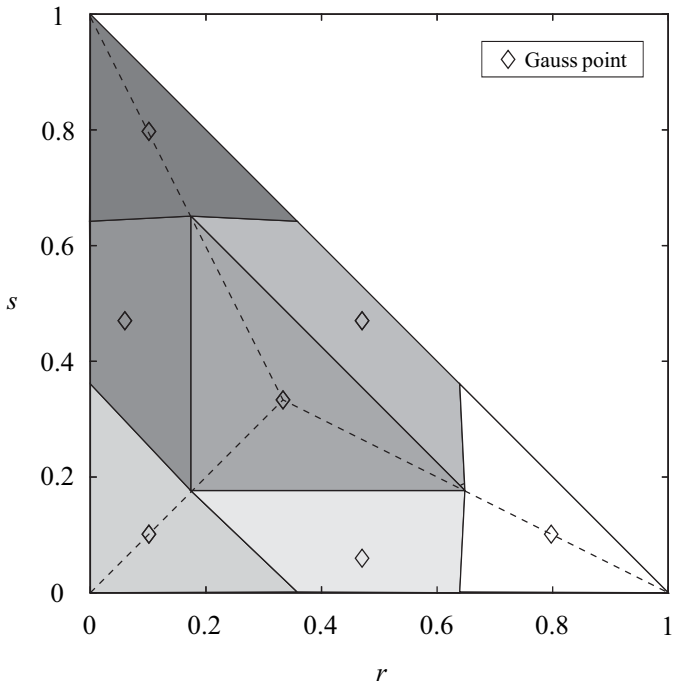

Figure 5.6 The membrane strain fields of the MITC3+S shell finite element (ver. 2) and the spatial distribution of the 7 Gauss points that the MITC3+S shell finite element (ver. 2) uses

5.3. Basic numerical tests

In this chapter, the three basic numerical tests are considered: the isotropy test, the patch tests and the zero energy mode test. The details about the basic numerical tests are given in Chapter 2.4 and Figure 2.1.

The isotropy test is performed. The MITC3+S shell finite element gives the identical results regardless of the node numbering sequences. The membrane, shearing and bending patch tests are performed. The MITC3+S shell finite element gives a constant stress at all points on the mesh. The zero energy mode test is performed. The MITC3+S shell finite element poses exactly six zero eigenvalues corresponding to the six physical rigid body modes. In conclusion, the smoothed 3-node triangular finite element passes all the basic numerical tests.

5.4. Convergence studies

In this chapter, convergence studies using appropriate benchmark problems are considered to verify the convergence behavior of the MITC3+S shell finite element compared to the MITC3+ shell finite element. The benchmark problems are listed in Table 5.1.

In the case of the Cook's skew beam problem, the normalized displacement is used to measure the error in the finite element solution. In the case of the other problems, the s-norm proposed by Hiller and Bathe [24] is used:

$$\left\|\vec{u}-\vec{u}_h\right\|_s^2=\int_\Omega \Delta\vec{\varepsilon}^T\Delta\vec{\tau}\,d\Omega \quad \text{with} \quad \Delta\vec{\varepsilon}=\vec{\varepsilon}-\vec{\varepsilon}_h,\ \Delta\vec{\tau}=\vec{\tau}-\vec{\tau}_h, \tag{5.27}$$

where $\vec{u}$ is the exact solution, $\vec{u}_h$ is the solution of the finite element discretization, $\vec{\varepsilon}$ is the strain vectors and $\vec{\tau}$ is the stress vectors. However, since it is difficult to obtain an exact solution for most problems, an well-converged finite element solution $\vec{u}_{ref}$ is used instead of the exact solution $\vec{u}$. To consider the various shell thicknesses, the relative error E_h is used:

$$E_h=\frac{\left\|\vec{u}_{ref}-\vec{u}_h\right\|_s^2}{\left\|\vec{u}_{ref}\right\|_s^2}. \tag{5.28}$$

The s-norm is appropriate to identify the finite elements satisfy the consistency and inf-sup conditions.

The optimal convergence behavior of the finite elements is given by [2]

$$E_h\cong Ch^k, \tag{5.29}$$

where h is the element size, and C is a constant independent on the h and the thickness but dependent on the material properties and the kind of finite element used. $k=2$ for 3-node triangular shell finite elements.

In the convergence studies, the distorted meshes are composed as follows. In the case of the $N\times N$ mesh, each edge is discretized at the ratio $L_1:L_2:L_3:.....L_N=1:2:3:.....N$, see Figure 5.7.

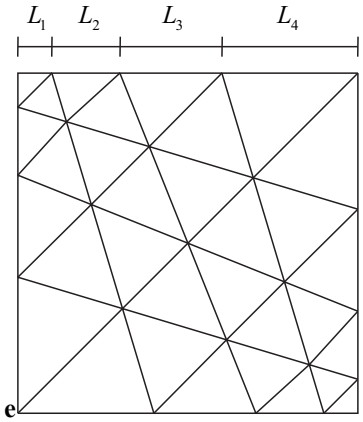

Figure 5.7 Distorted mesh (4×4 mesh)

Table 5.1 List of the benchmark problems

Benchmark problems	Boundary condition	Shell behavior	Mesh pattern
Cook's skew beam	Left end clamped	Membrane-dominated	Regular
			Distorted
Square plate	All edges clamped	Bending-dominated	Regular
			Distorted
Scordelis-Lo roof shell	Both ends diaphragm	Mixed	Regular
			Distorted
Cylindrical shell	Both ends clamped	Membrane-dominated	Regular
			Distorted
	Both ends free	Bending-dominated	Regular
			Distorted
Hyperboloid shell	Both ends clamped	Membrane-dominated	Regular
			Distorted
	Both ends free	Bending-dominated	Regular
			Distorted

5.4.1. Cook's skew beam problem

The 2D plane stress Cook's skew beam problem shown in Figure 5.8 is considered. The length of the beam is $L = 48\text{m}$, the length of the left end is $H_1 = 44\text{m}$ and the length of the right end is $H_2 = 16\text{m}$. The distributed shear load $p_0 = 1/16\,\text{N/m}$ is applied on the right end and the left end is clamped. The Young's modulus is $E = 1\text{N/m}^2$; the Poisson ratio is $\nu = 1/3$.

The deflection at point A is calculated using the MITC3+ shell finite element and the MITC3+S shell finite element obtained with $N \times N$ meshes (N = 2, 4, 8 and 16), see Figure 5.9. The reference solution is obtained using 32×32 mesh of the MITC9 shell finite element.

In these problem solutions, since this problem corresponds to a membrane-dominated problem, the convergence behaviors are further improved in the order of the MITC3+ shell finite element, the first version of the MITC+S shell finite element and the second version of the MITC3+S shell finite element.

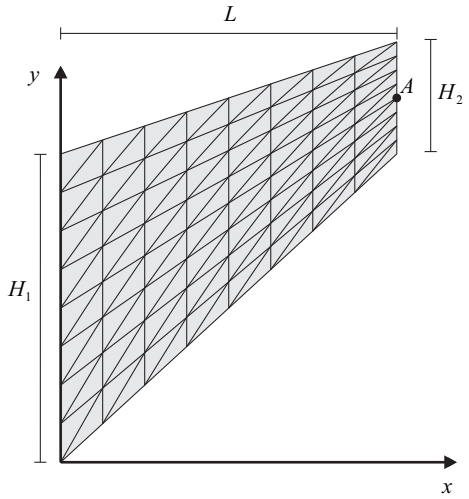

Figure 5.8 Cook's skew beam problem

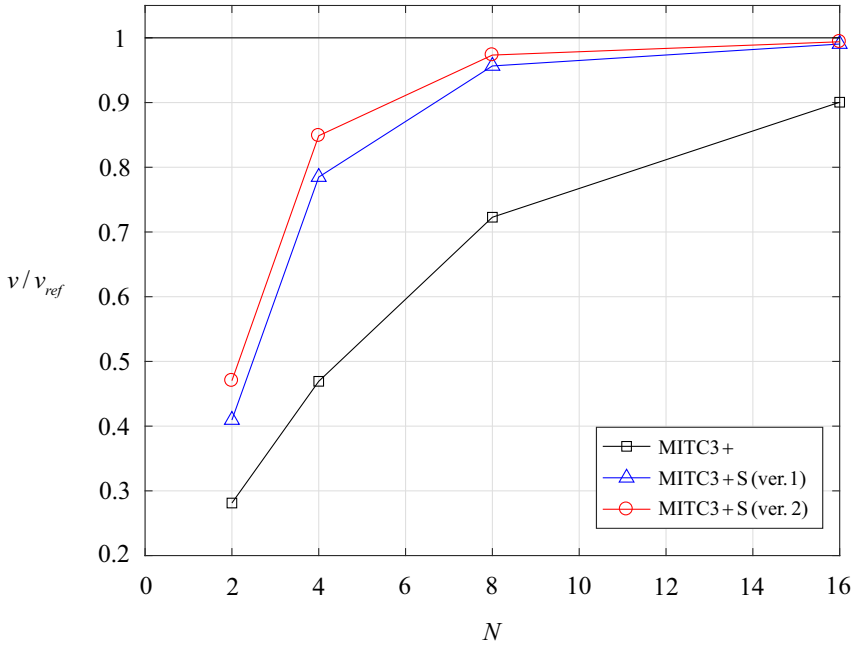

Figure 5.9 Normalized deflection v/v_{ref} at point A

5.4.2. Square plate problem

The plate bending problem shown in Figure 5.10 is considered. The length of the edges of the square plate is $2L = 2\text{m}$; it has a uniform thickness t. The square plate is subjected to a uniform pressure $p_0 = 1\text{N/m}^2$. The clamped boundary conditions are imposed on all the edges. Due to symmetry, only a one-quarter model is considered, with the following boundary conditions: $u_x = \theta_y = 0$ along AB, $u_y = \theta_x = 0$ along AC and $u_x = u_y = u_z = \theta_x = \theta_y = 0$ along BD and CD.

The reference solutions are obtained using 32×32 mesh of the MITC9 shell finite element. The solutions using the MITC3+ shell finite element and the MITC3+S shell finite element are obtained with $N \times N$ meshes ($N = 4$, 8, 16 and 32). The element size is $h = L / N$. The Young's modulus is $E = 3.0 \times 10^7\ \text{N/m}^2$; the Poisson ratio is $\nu = 0.3$. The range of $t / L =$ 1/100, 1/1000 and 1/10000 is considered.

Figure 5.11 give the convergence curves for the regular meshes and Figure 5.12 give the convergence curves for the distorted meshes. In these problem solutions, since this problem corresponds to a bending-dominated problem, the MITC+ shell finite element, the first version of the MITC3+S shell finite element and the second version of the MITC3+S shell finite element present similarly good convergence behaviors.

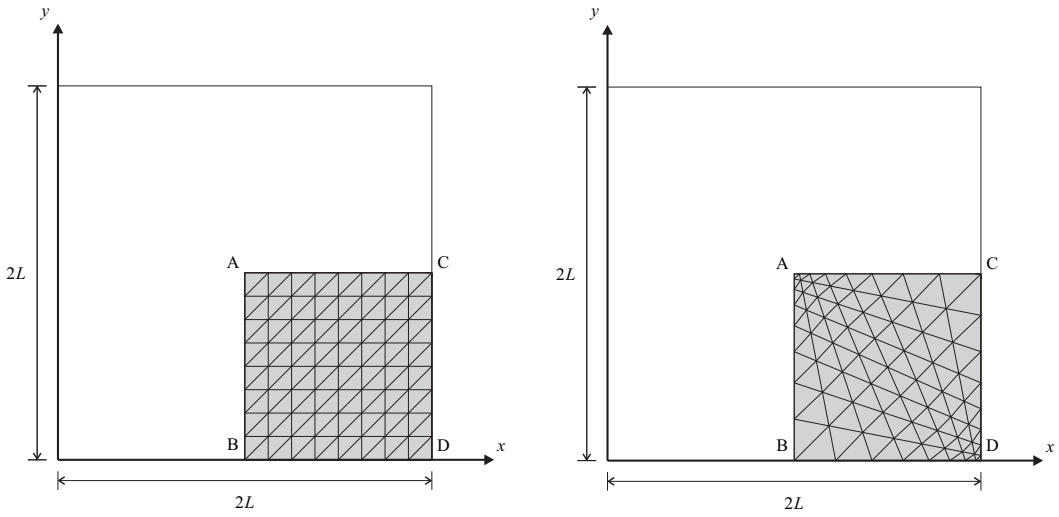

Figure 5.10 Square plate problem

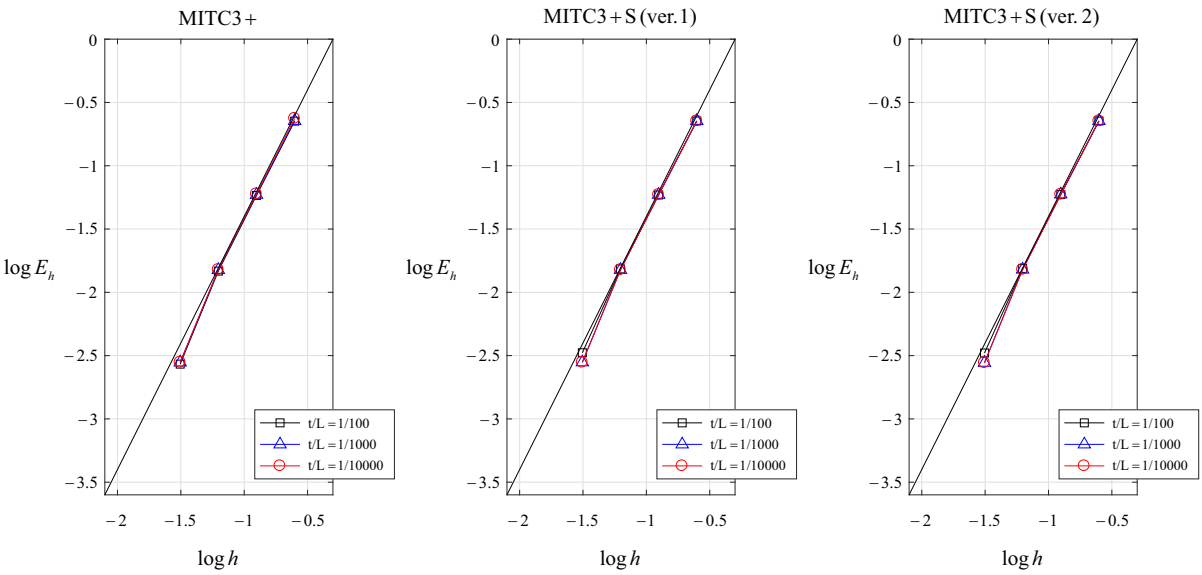

Figure 5.11 Convergence curves for the square plate problem with the regular meshes

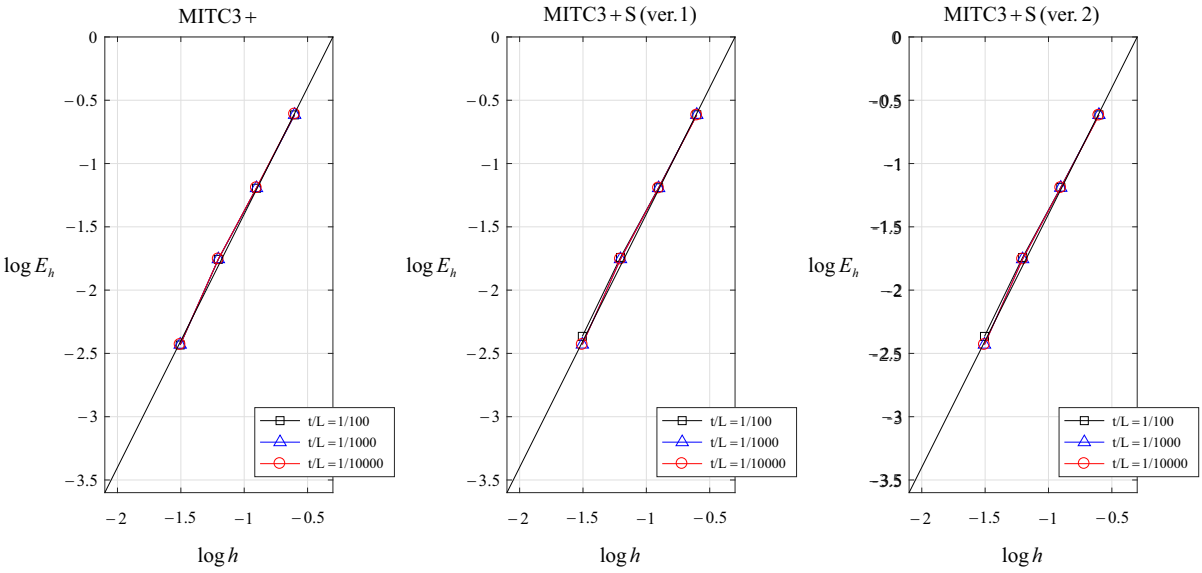

Figure 5.12 Convergence curves for the square plate problem with the distorted meshes

5.4.3. Scordelis-Lo roof shell problem

The Scordelis-Lo roof shell problem shown in Figure 5.13 is considered. The shell is a segment of a cylinder. The length of the cylinder is $2L = 2\text{m}$; the radius of the cylinder is $R = 1\text{m}$; it has a uniform thickness t. The shell is subjected to a self-weight loading $f_z = 1\text{N/m}^2$. Diaphragm boundary conditions are imposed on both ends. Due to symmetry, only a one-quarter model is considered with the following boundary conditions: $u_x = u_z = 0$ along AC, $u_y = \alpha = 0$ along BD and $u_x = \beta = 0$ along CD.

The reference solutions are obtained using 32×32 mesh of the MITC9 shell finite element. The solutions using the MITC3+ shell finite element and the MITC3+S shell finite element are obtained with $N \times N$ meshes (N = 4, 8, 16 and 32). The element size is $h = L / N$. The Young's modulus is $E = 3.0 \times 10^7\ \text{N/m}^2$; the Poisson ratio is $\nu = 0.3$. The range of t / L = 1/100, 1/1000 and 1/10000 is considered.

Figure 5.14 give the convergence curves for the regular meshes and Figure 5.15 give the convergence curves for the distorted meshes. In these problem solutions, since this problem corresponds to a mixed problem, the convergence behaviors are further improved in the order of the MITC3+ shell finite element, the first version of the MITC+S shell finite element and the second version of the MITC3+S shell finite element.

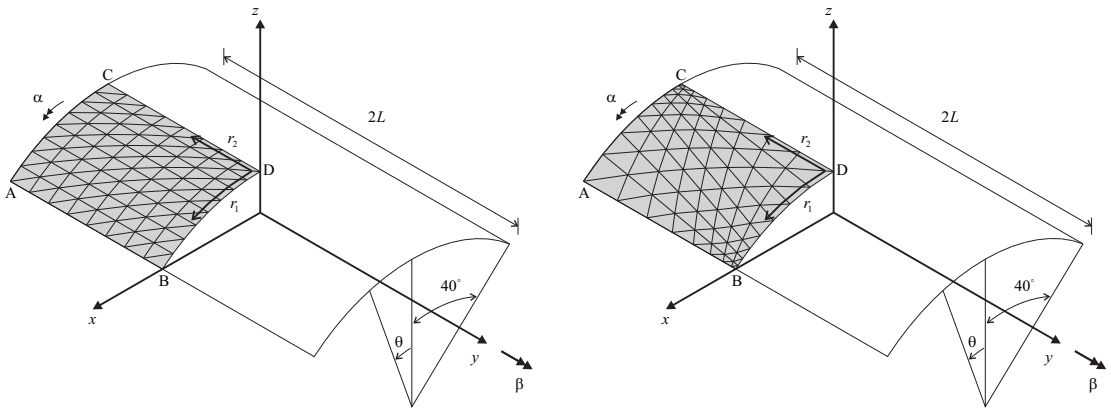

Figure 5.13 Scordelis-Lo roof shell problem

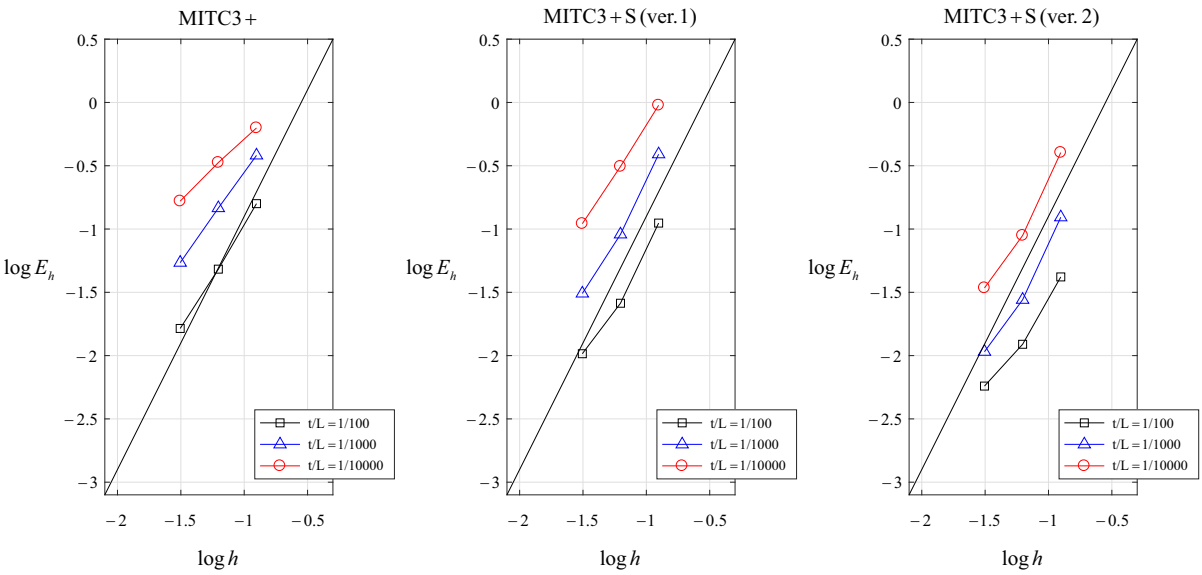

Figure 5.14 Convergence curves for the Scordelis-Lo roof shell problem with the regular meshes

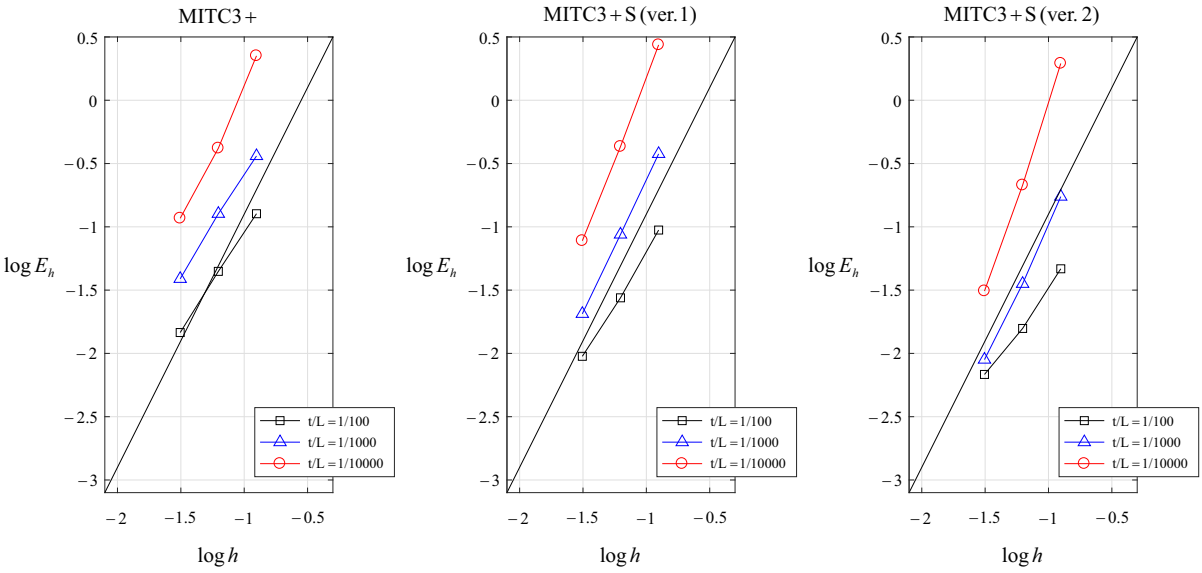

Figure 5.15 Convergence curves for the Scordelis-Lo roof shell problem with the distorted meshes

5.4.4. Cylindrical shell problems

The cylindrical shell problems shown in Figure 5.17 are considered. The length of the cylinder is $2L = 2\text{m}$; the radius of the cylinder is $R = 1\text{m}$; it has a uniform thickness t . The shell is subjected to a varying pressure $p(\theta) = p_0 \cos(2\theta)$, see Figure 5. 16.

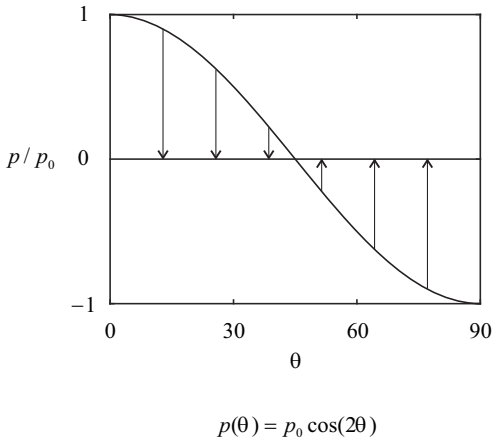

Figure 5.16 Profile of the pressure

This shell structure shows different asymptotic behaviors depending on the boundary conditions at its ends. When both ends are clamped, a membrane dominated problem is considered, whereas when both ends are free, a bending dominated problem is considered.

Using symmetry, only a one-eighth model is considered. To have the membrane-dominated problem, the clamped boundary conditions are imposed: $u_x = \beta = 0$ along BD, $u_z = \beta = 0$ along AC, $u_y = \alpha = 0$ along AB and $u_x = u_y = u_z = \alpha = \beta = 0$ along CD. To have the bending-dominated problem, the free boundary conditions are imposed: $u_x = \beta = 0$ along BD, $u_z = \beta = 0$ along AC and $u_y = \alpha = 0$ along AB.

The reference solutions are obtained using 32×32 mesh of the MITC9 shell finite element. The solutions using the MITC3+ shell finite element and the MITC3+S shell finite element are obtained with $N \times N$

meshes (N = 4, 8, 16 and 32). The element size is $h = L / N$. The Young's modulus is $E = 3.0 \times 10^7 \text{ N/m}^2$; the Poisson ratio is $\nu = 0.3$. The range of t / L = 1/100, 1/1000 and 1/10000 is considered.

Figure 5.18 give the convergence curves of the clamped cases for the regular meshes, Figure 5.19 give the convergence curves of the clamped cases for the distorted meshes, Figure 5.20 give the convergence curves of the free cases for the regular meshes and Figure 5.21 give the convergence curves of the free cases for the distorted meshes. In the clamped cases, since this problem corresponds to a membrane-dominated problem, the convergence behaviors are further improved in the order of the MITC3+ shell finite element, the first version of the MITC+S shell finite element and the second version of the MITC3+S shell finite element. In the free cases, since this problem corresponds to a bending-dominated problem, the MITC3+ shell finite element, the first version of the MITC3+S shell finite element and the second version of the MITC3+S shell finite element present similarly good convergence behaviors.

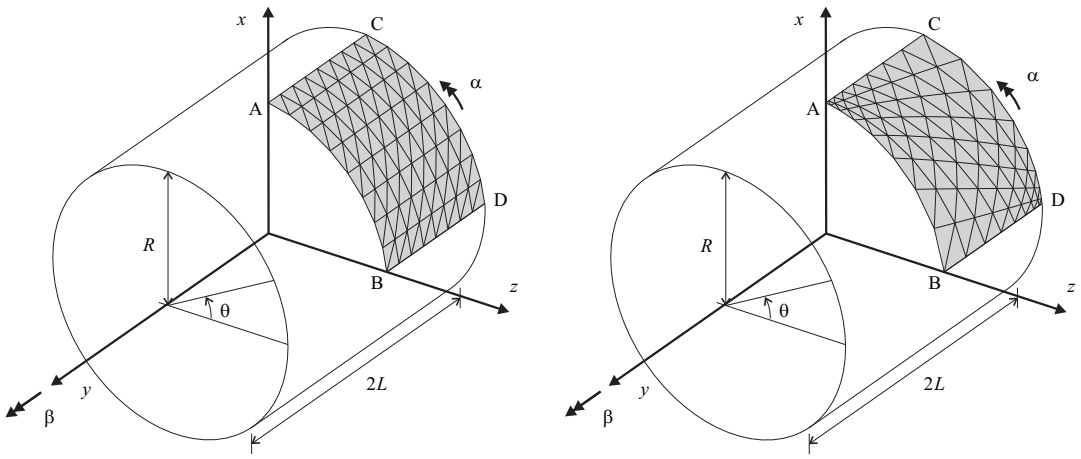

Figure 5.17 Cylindrical shell problems

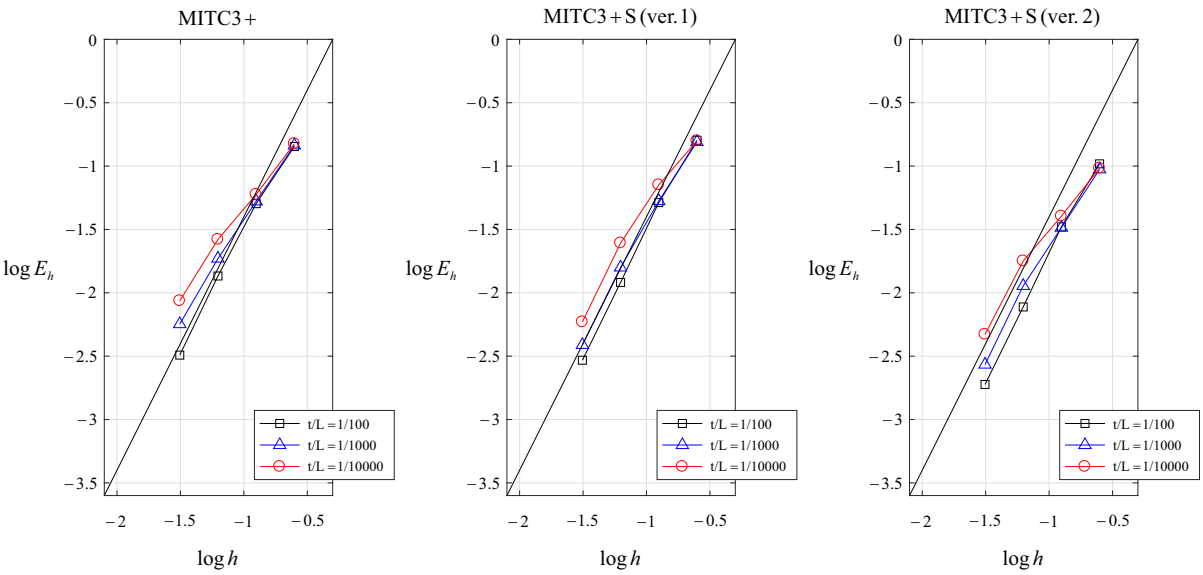

Figure 5.18 Convergence curves for the clamped cylindrical shell problem with the regular meshes

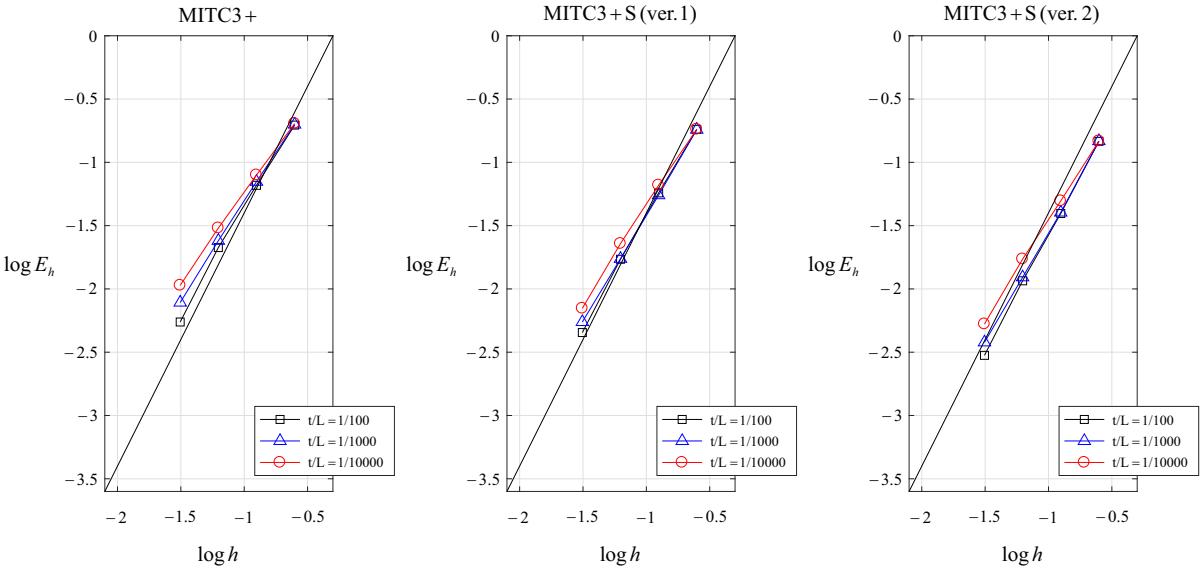

Figure 5.19 Convergence curves for the clamped cylindrical shell problem with the distorted meshes

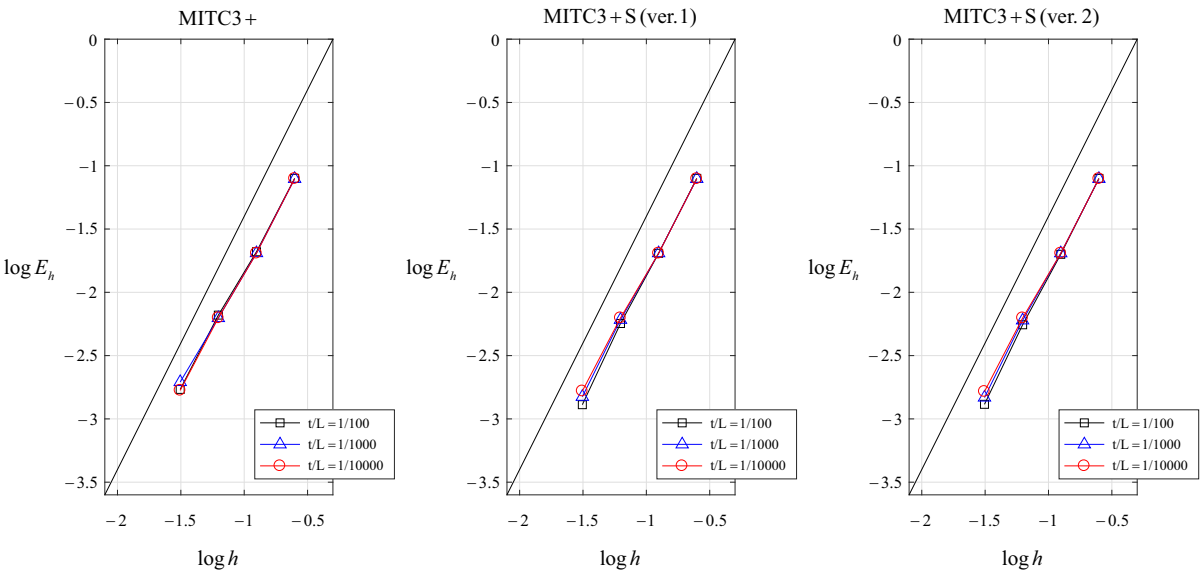

Figure 5.20 Convergence curves for the free cylindrical shell problem with the regular meshes

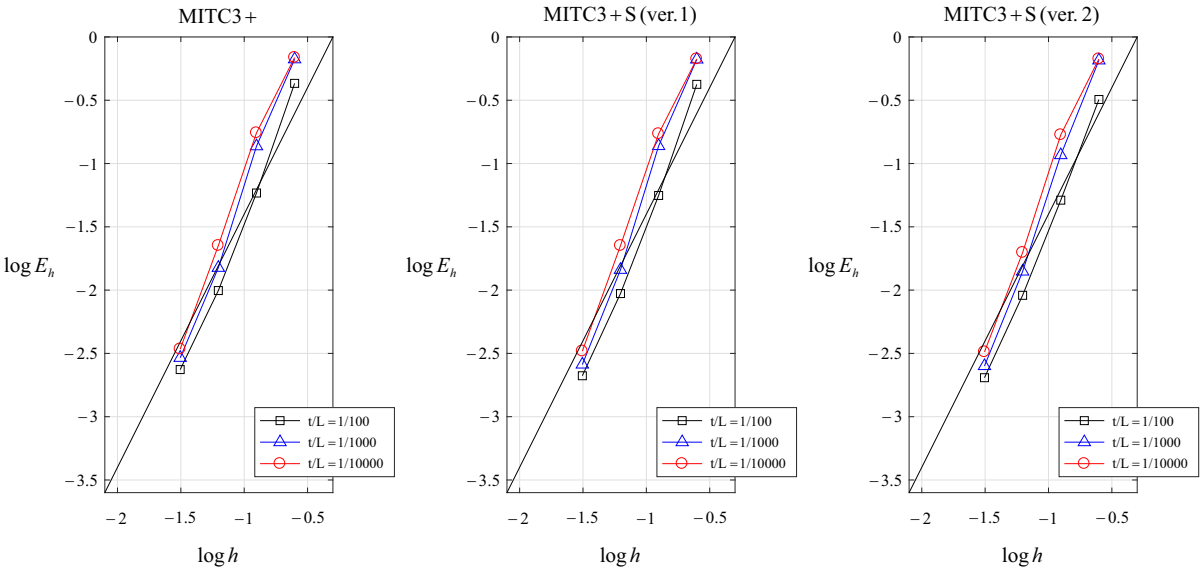

Figure 5.21 Convergence curves for the free cylindrical shell problem with the distorted Meshes

5.4.5. Hyperboloid shell problems

The hyperboloid shell problem shown in Figure 5.22 are considered. The mid-surface of the shell is given by

$$x^2 + z^2 = 1 + y^2, \quad y \in [-1, 1]; \tag{5.30}$$

it has a uniform thickness t. The shell is subjected to a varying pressure $p(\theta) = p_0 \cos(2\theta)$, see Figure 5. 16.

This shell structure shown different asymptotic behaviors depending on the boundary conditions at its end. When both ends are clamped, a membrane dominated problem is considered, whereas when both ends are free, a bending dominated problem is considered.

Using symmetry, only a one-eighth model is considered. To have the membrane-dominated problem, the clamped boundary conditions are imposed: $u_x = \beta = 0$ along BD, $u_z = \beta = 0$ along AC, $u_y = \alpha = 0$ along AB and $u_x = u_y = u_z = \alpha = \beta = 0$ along CD. To have the bending-dominated problem, the free boundary conditions are imposed: $u_x = \beta = 0$ along BD, $u_z = \beta = 0$ along AC and $u_y = \alpha = 0$ along AB.

The reference solutions are obtained using 32×32 mesh of the MITC9 shell finite element. The solutions using the MITC3+ shell finite element and the MITC3+S shell finite element are obtained with $N \times N$ meshes (N = 4, 8, 16 and 32). The element size is $h = L / N$. The Young's modulus is $E = 3.0 \times 10^7$ N/m^2; the Poisson ratio is $\nu = 0.3$. The range of t / L = 1/100, 1/1000 and 1/10000 is considered.

Figure 5.23 give the convergence curves of the clamped cases for the regular meshes, Figure 5.24 give the convergence curves of the clamped cases for the distorted meshes, Figure 5.25 give the convergence curves of the free cases for the regular meshes and Figure 5.26 give the convergence curves of the free cases for the distorted meshes. In the clamped cases, since this problem corresponds to a membrane-dominated problem, the convergence behaviors are further improved in the order of the MITC3+ shell finite element, the first version of the MITC+S shell finite element and the second version of the MITC3+S shell finite element. In the free cases,

since this problem corresponds to a bending-dominated problem, the MITC3+ shell finite element, the first version of the MITC3+S shell finite element and the second version of the MITC3+S shell finite element present similarly good convergence behaviors.

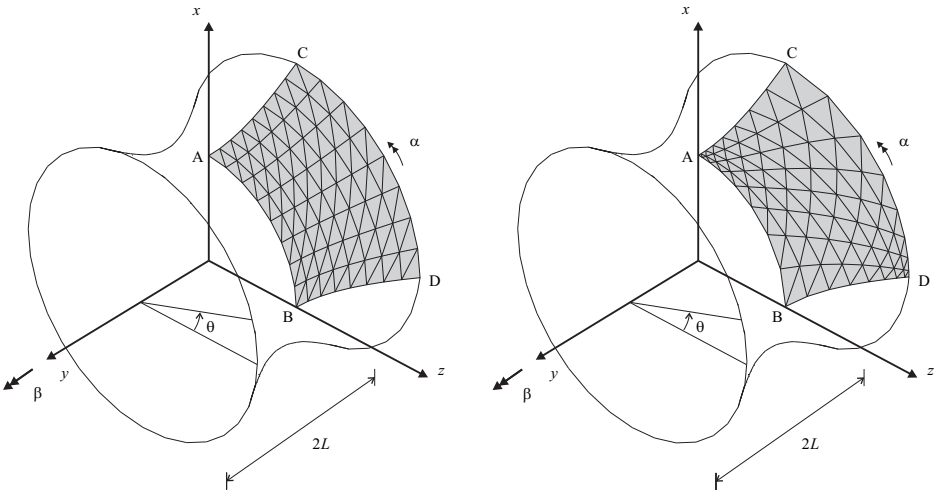

Figure 5.22 Hyperboloid shell problems

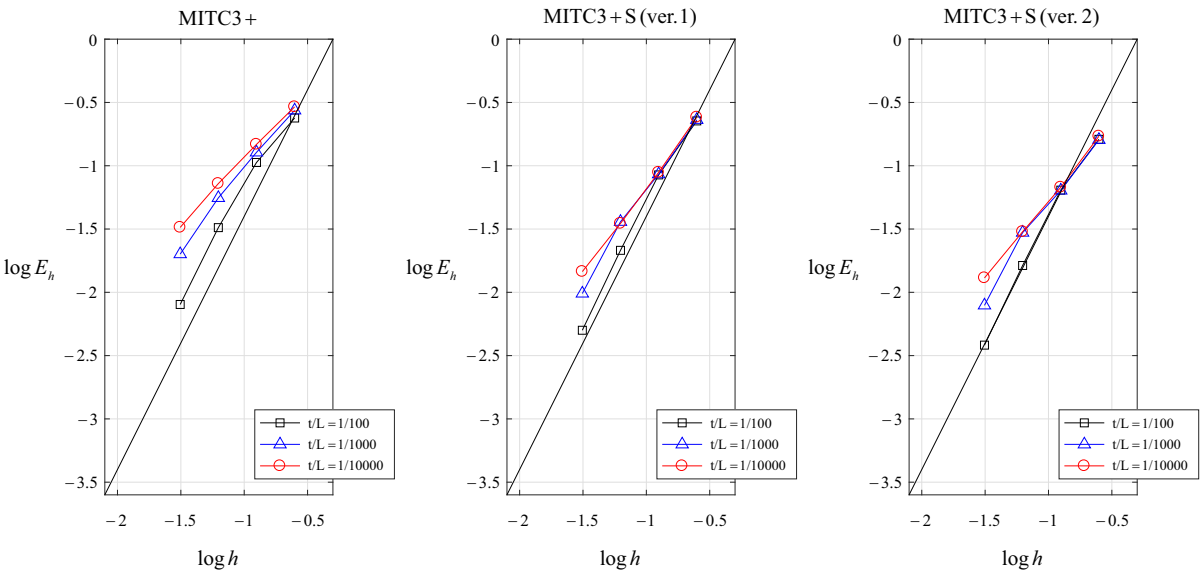

Figure 5.23 Convergence curves for the clamped hyperboloid shell problem with the regular meshes

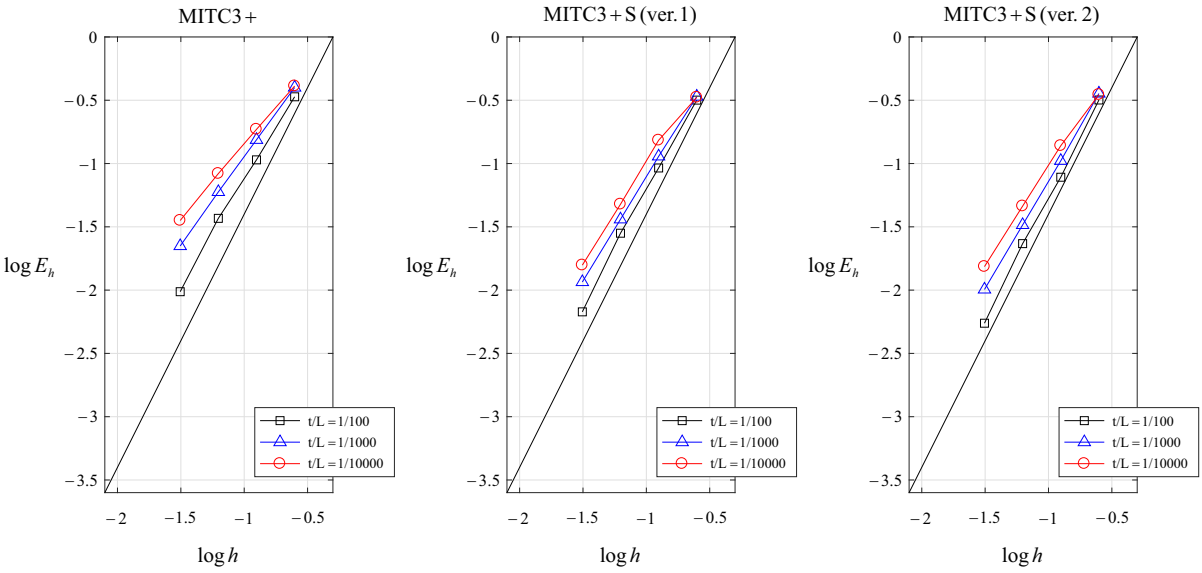

Figure 5.24 Convergence curves for the clamped hyperboloid shell problem with the distorted meshes

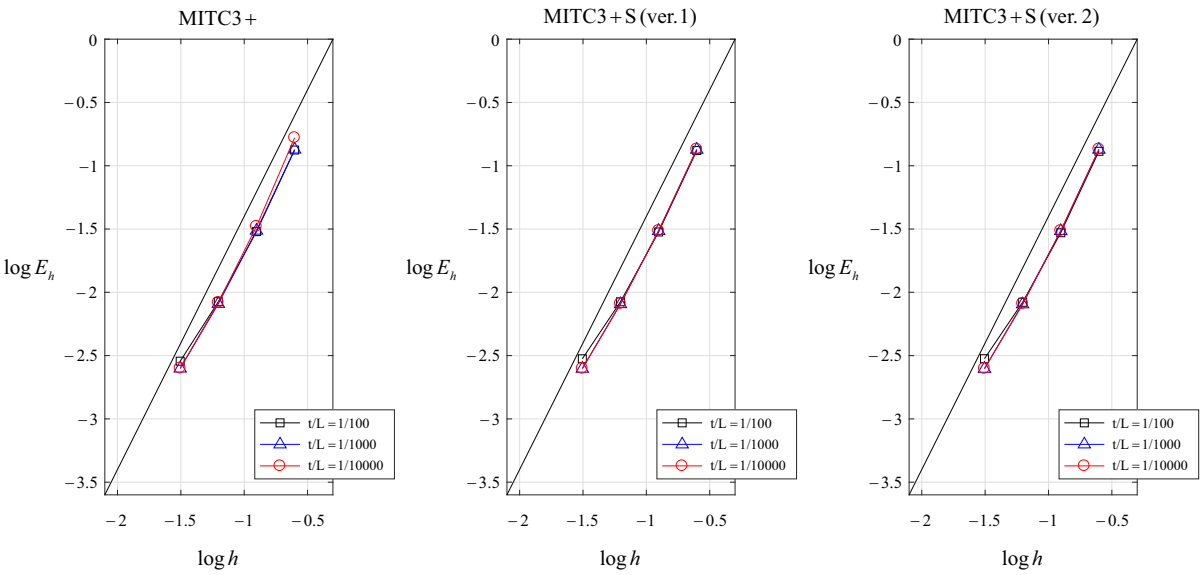

Figure 5.25 Convergence curves for the free hyperboloid shell problem with the regular meshes

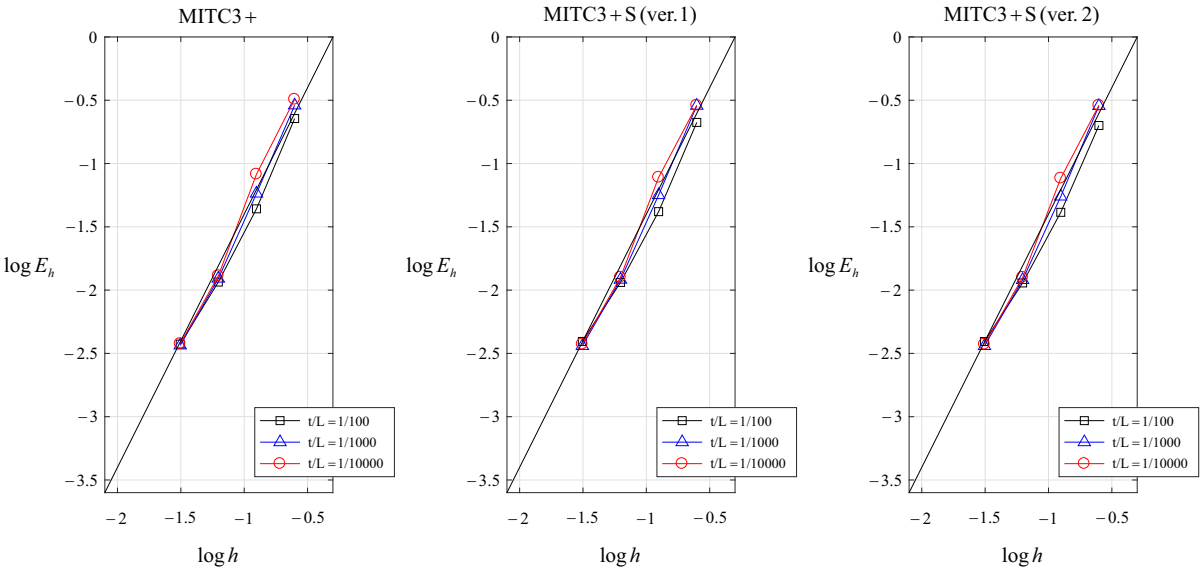

Figure 5.26 Convergence curves for the free hyperboloid shell problem with the distorted meshes

Chapter 6. Conclusions

The purpose of this thesis is to improve the membrane performance of the MITC3+ shell finite element using the strain smoothing technique. The MITC3+ shell finite element has an outstanding convergence behavior in bending-dominated problems. However, there is no difference in membrane performance from the 3-node triangular displacement-based shell finite element (DISP3).

In this paper, a new 3-node triangular shell finite element named MITC3+S has been developed that improves the membrane performance of the MITC3+ shell finite element. The first version of the MITC3+S shell finite element has contributed to the successful application of the edge-based strain smoothing technique to the continuum mechanics based MITC3+ shell finite element. The first version has successfully improved the membrane performance of the MITC3+ shell finite element. However, the first version increases the number of the integration points by 3 times even if it doesn't increase the number of degrees of freedom.

The second version of the MITC3+S shell finite element has been developed which alleviates the problem of increasing computation time in the first version and has even better membrane performance than the first version. The enhanced edge-based strain smoothing technique has been developed and utilized in the process of the study.

The MITC3+S shell finite element presents isotropic behavior and pass the consistency, ellipticity and inf-sup conditions. The MITC3+S shell element shows an improved convergence behavior in various benchmark problems.

Bibliography

[1] P. S. LEE, K. J. BATHE, “On the asymptotic behavior of shell structures and the evaluation in finite element solutions,” Computers and Structures, 80, 235-255 (2002)

[2] K. J. BATHE, “Finite element procedures,” New York, Prentice Hall (1996)

[3] K. J. BATHE, E. N. DVORKIN, “A formulation of general shell elements – the use of mixed interpolation of tensorial components,” International Journal for Numerical Methods in Engineering, 22, 697-722 (1986)

[4] M. L. BUCALEM, K. J. BATHE, “Higher-order MITC general shell elements,” International Journal for Numerical Methods in Engineering, 36, 3729-3754 (1993)

[5] P. S. LEE, K. J. BATHE, “Development of MITC isotropic triangular shell finite elements,” Computers and Structures, 82, 945-962 (2004)

[6] Y. LEE, P. S. LEE, K. J. BATHE, “The MITC3+ shell element and its performance,” Computers and Structures, 138, 12-23 (2014)

[7] Y. LEE, H. M. JEON, P. S. LEE, K. J. BATHE, “The modal behavior of the MITC3+ triangular shell element,” Computers and Structures, 153, 148-164 (2015)

[8] H. M. JEON, Y. LEE, P. S. LEE, K. J. BATHE, “The MITC3+ shell element in geometric nonlinear analysis,” Computers and Structures, 146, 91-104 (2015)

[9] J. S. CHEN, C. T. WU, S. YOON, Y. YOU, “A stabilized conforming nodal integration for Galerkin mesh-free methods,” International Journal for Numerical Methods in Engineering, 50. 435-466 (2001)

[10] G. R. LIU, T. NGUYEN-THOI, H. NGUYEN-XUAN, K. Y. LAM, “A node-based smoothed finite element method (NS-FEM) for upper bound solutions to solid mechanics problem,” Computers and Structures, 87, 14-26 (2009)

[11] G. R. LIU, T. NGUYEN-THOI, K. Y. LAM, “An edge-based smoothed finite element Method (ES-FEM) for Static, Free and Forced Vibration Analysis of Solids,” Journal of Sound and Vibration, 320, 1100-1130 (2009).

[12] T. NGUYEN-THOI, P. PHUNG-VAN, C. THAI.HOANG, H. NGUYEN-XUAN, “A Cell-based smoothed shear gap method (CS-DSG3) using triangular elements for static and free vibration analyses of shell structures,” International Journal of Mechanical Sciences, 74, 32-45, (2013)

[13] H. NGUYEN-XUAN, G. R. LIU, C. THAI-HOANG, T. NGUYEN-THOI, “An edge-based smoothed finite element method (ES-FEM) with stabilized discrete shear gap technique for analysis of Reissner-Mindlin plates,” Comput. Methods Appl. Mech. Engrg., 199, 471-489 (2010)

[14] X. CUI, G. R. LIU, G. LI, G. Y. ZHANG G. ZHENG, “Analysis of plates and shells using an edge-based smoothed finite element method,” Comput. Mech., 45, 141-156 (2010)

[15] C. M. SHIN, B. C. LEE, “Development of a strain-smoothed three-node triangular flat shell element with drilling degrees of freedom,” Finite Elements in Analysis and Design, 86, 71-80 (2014)

[16] D. SOHN, J. HAN, Y. S. CHO, S. IM, “A finite element scheme with the aid of a new carving technique combined with smoothed integration.” Computer Methods in Applied Mechanics and Engineering, 254, 42-60 (2013)

[17] S. JIN, D. SOHN, S. IM, “Node-to-node scheme for three-dimensional contact mechanics using polyhedral type variable-node elements,” Computer Methods in Applied Mechanics and Engineering, 304, 217-242 (2016)

[18] O. ZIENKIEWICZ, R. TAYLOR, J. TOO, “Reduced integration technique in general analysis of plates and shells, International Journal for Numerical Methods in Engineering, 3, 275-90 (1971)

[19] K. U. BLETZINGER, M. BISCHOFF, E. RAMM, “A unified approach for shear-locking-free triangular and rectangular shell finite elements,” Computer and Structures, 75, 321-334 (2000)

[20] M. BISCHOFF, K. BLETZINGER, “Stabilized DSG plate and shell elements,” Trends in Computational Structural Mechanics, 253-63 (2001)

[21] P. S. LEE, H. C. NOH, K. J. BATHE, “Insight into 3-node triangular shell finite elements: the effects of element isotropy and mesh patterns,” Computers and Structures, 85, 404-418 (2007)

[22] S. P. TIMOSHENKO, J. N. GOODIER, “Theory of elasticity,” New York, McGraw-Hill (1970)

[23] Y. KO, P. S. LEE, K. J. BATHE, “The MITC4+ shell element and its performance,” Computers and Structures, 169, 57-68 (2016)

[24] J. F. HILLER, K. J. BATHE, “Measuring convergence of mixed finite element discretizations: an application to shell structures,” Computers and Structures, 81, 639-654 (2003)